

2014

## Investigation of Dimensionality-Dependent Foam Rheological Properties by Using Mechanistic Foam Model

Woochan Lee

*Louisiana State University and Agricultural and Mechanical College*

Follow this and additional works at: [https://digitalcommons.lsu.edu/gradschool\\_theses](https://digitalcommons.lsu.edu/gradschool_theses)



Part of the [Petroleum Engineering Commons](#)

---

### Recommended Citation

Lee, Woochan, "Investigation of Dimensionality-Dependent Foam Rheological Properties by Using Mechanistic Foam Model" (2014). *LSU Master's Theses*. 3609.

[https://digitalcommons.lsu.edu/gradschool\\_theses/3609](https://digitalcommons.lsu.edu/gradschool_theses/3609)

This Thesis is brought to you for free and open access by the Graduate School at LSU Digital Commons. It has been accepted for inclusion in LSU Master's Theses by an authorized graduate school editor of LSU Digital Commons. For more information, please contact [gradetd@lsu.edu](mailto:gradetd@lsu.edu).

# INVESTIGATION OF DIMENSIONALITY-DEPENDENT FOAM RHEOLOGICAL PROPERTIES BY USING MECHANISTIC FOAM MODEL

A Thesis

Submitted to the Graduate Faculty of the  
Louisiana State University and  
Agricultural and Mechanical College  
in partial fulfillment of the  
requirements for the degree of  
Master of Science in Petroleum Engineering

in

The Craft & Hawkins Department of Petroleum Engineering

by

Woochan Lee

B.S., University of Texas at Austin, 2010

December 2014

©Copyright 2014  
Woochan Lee  
All rights reserved

## **ACKNOWLEDGEMENTS**

It has been my honor to be a graduate student in the Craft and Hawkins Department of Petroleum Engineering at Louisiana State University and I appreciate people who supported me to learn and accomplish the degree. I would like to thank Dr. Seung Kam for his guidance, help, and inspiration during the program and for the belief in my capability for the project. I would also thank to Dr. Clinton Willson and Dr. Stephen Sears for their valuable suggestions and comments to this thesis. I am also thankful to Daewoo Shipbuilding & Marine Engineering, Blackhorse energy LLC, and the Department for providing financial supports during this research. Last, but not least, I want to thank my wife, Juyun Lee, and family for their countless support, love, and encouragement that enabled me complete my work.

## TABLE OF CONTENTS

ACKNOWLEDGEMENTS.....	iii
LIST OF TABLES.....	v
LIST OF FIGURES.....	vi
ABSTRACT .....	ix
CHAPTER 1. INTRODUCTION .....	1
1.1 Background of This Study .....	1
1.2 Motivation and Objectives of This Study.....	2
1.3 Chapter Description.....	2
CHAPTER 2. LITERATURE REVIEW .....	3
2.1 Introduction of Foams .....	3
2.2 Recent Developments: “two steady-state foam-flow regimes” and “three foam states” ..	8
CHAPTER 3. METHODOLOGY .....	12
3.1 Mechanistic foam model and model parameters .....	12
3.2 Discretization of the system .....	17
CHAPTER 4. RESULTS AND DISCUSSIONS .....	19
4.1 Base case and its extension .....	22
4.2. Effect of input parameters .....	34
4.3. Implications in field-scale foam processes .....	41
CHAPTER 5. CONCLUSIONS.....	52
REFERENCES.....	54
VITA.....	57

## LIST OF TABLES

Table 4.1 Model parameters and properties used in this study (following Afsharpoor et al., 2010) .....	20
Table 4.2 Description of a radial system for base-case calculation.....	23
Table 4.3 Foam field tests with injection condition .....	41

## LIST OF FIGURES

Fig. 2.1 Three in-situ lamella-creation mechanisms (from Ransohoff et al. (1988)) .....	6
Fig. 2.2 Disjoining pressure curve ( $\Pi$ ) as a function of foam film thickness ( $h$ ), demonstrating minimum film thickness for stability ( $h_{cr}$ ) and corresponding maximum disjoining pressure ( $\Pi_{max}$ ) (from Miller and Neogi (1985)) .....	6
Fig. 2.3 A contour map showing two distinct foam flow regimes obtained from laboratory flow experiments (from Osterloh and Jante (1992)) .....	10
Fig. 2.4 A schematic figure showing three different foam states such as weak-foam (or coarse-foam), strong-foam and intermediate states (from Gauglitz et al. (2002)) .....	10
Fig. 2.5 An S-shaped foam-generation curve showing three different foam states (from Kam and Rossen (2003)) .....	11
Fig. 2.6 A contour map showing two steady-state strong-foam regimes reconstructed by Kam and Rossen (2003) by using mobilization pressure gradient concept .....	11
Fig. 3.1 The rate of lamella creation (from Kam, 2008) and the rate of lamella coalescence (from Afsharpoor et al., 2010) used in this study .....	14
Fig. 3.2 A schematic of radial system of interest (only a quarter is shown for simplicity) .....	18
Fig. 4.1 Foam rheology plots reproduced by the model using model inputs in Table 4.1: (a) S-shaped curve ( $\nabla P$ vs. $u_g$ ) at fixed $u_w = 1.0 \times 10^{-6}$ m/s and (b) two-flow-regime map .....	20
Fig. 4.2 Three-dimensional foam-rheology surface constructed by a series of S-shaped curves ( $\nabla P$ vs. $u_t$ at fixed $f_g$ ) at various injection foam qualities .....	21
Fig. 4.3 Two-dimensional view of 3D plot shown in Fig. 4.2 ( $\nabla P$ vs. $u_t$ at fixed $f_g$ ) .....	21
Fig. 4.4 A small-scale radial system investigated as a base case .....	23
Fig. 4.5 Change in total injection velocity ( $u_t$ ) as a function of radial distance ( $r$ ) .....	24
Fig. 4.6 S-shape curve at $f_g = 0.80$ representing six segments of the base case .....	24
Fig. 4.7 Mechanistic foam fractional flow curves at 6 different grid blocks represented by Fig. 4.4 (total injection rate ( $q_t$ ) = $1.33 \times 10^{-5}$ m <sup>3</sup> /s and injection foam quality = 0.80) .....	25
Fig. 4.8 How to find MRF values to fit foam mobility obtained by mechanistic foam fractional flow curve at $u_t = 6.33 \times 10^{-5}$ m/s and $f_g = 0.80$ .....	26

- Fig. 4.9 Base-case calculation results showing the steady state after foam flooding (strong foams in the low-quality regime injected): (a) water saturation ( $S_w$ ); (b) pressure ( $P$  and  $\nabla P$ ); (c) mobility ( $k_{rg}^f/\mu_g^f$ ); and (d) mobility reduction factor (MRF)..... 27
- Fig. 4.10 Base-case calculation results showing the steady state after foam flooding (strong foams in the low-quality regime injected): (a) trapped gas fraction ( $X_t$ ); (b) foam texture ( $n_f$ ); (c) foam relative permeability ( $k_{rg}^f$ ); and (d) foam viscosity ( $\mu_g^f$ ) ..... 28
- Fig. 4.11 Extension of base case calculation results showing the steady state after foam flooding (strong foams in the high-quality regime injected): (a) water saturation ( $S_w$ ); (b) pressure ( $P$  and  $\nabla P$ ); (c) mobility ( $k_{rg}^f/\mu_g^f$ ); and (d) mobility reduction factor (MRF) ..... 29
- Fig. 4.12 Extension of base case calculation results showing the steady state after foam flooding (strong foams in the high-quality regime injected) (a) trapped gas fraction ( $X_t$ ); (b) foam texture ( $n_f$ ); (c) foam relative permeability ( $k_{rg}^f$ ); and (d) foam viscosity ( $\mu_g^f$ ) ..... 30
- Fig. 4.13 Extension of base case calculation results showing the steady state after foam flooding (weak foams injected): (a) water saturation ( $S_w$ ); (b) pressure ( $P$  and  $\nabla P$ ); (c) mobility ( $k_{rg}^f/\mu_g^f$ ); and (d) mobility reduction factor (MRF)..... 32
- Fig. 4.14 Extension of base case calculation results showing the steady state after foam flooding (weak foams injected): (a) trapped gas fraction ( $X_t$ ); (b) foam texture ( $n_f$ ); (c) foam relative permeability ( $k_{rg}^f$ ); and (d) foam viscosity ( $\mu_g^f$ )..... 33
- Fig. 4.15 Calculation results comparing three grid block sizes ( $\Delta r = 0.5, 1, \text{ and } 2$  inches): (a) water saturation and (b) mobility reduction factor ( $\Delta r = 2$  inch is selected in this study) ..... 34
- Fig. 4.16 Calculation results showing the steady state after foam flooding (strong foams injected) at various foam qualities: (a) water saturation ( $S_w$ ); (b) pressure gradient ( $\nabla P$ ); (3) MRF; and (4) foam texture ( $n_f$ )..... 35
- Fig. 4.17 Calculation results showing the steady state after foam flooding (strong foams in the low-quality regime injected;  $f_g = 0.80$ ) at various injection rates: (a) total injection velocity ( $u_t$ ); (b) water saturation ( $S_w$ ); (c) pressure gradient ( $\nabla P$ ); and (d) MRF ..... 37
- Fig. 4.18 Calculation results showing the steady state after foam flooding (strong foams in the high-quality regime injected;  $f_g = 0.99$ ) at various injection rates: (a) total injection velocity ( $u_t$ ); (b) water saturation ( $S_w$ ); (c) pressure gradient ( $\nabla P$ ); and (d) MRF ..... 38
- Fig. 4.19 Calculation results showing the steady state after foam flooding (strong foams injected;  $q_t = 1.33 \times 10^{-5} \text{ m}^3/\text{s}$  and  $f_g = 0.80$ ) at different systems: (a) total injection velocity ( $u_t$ ); (b) water saturation ( $S_w$ ); (c) pressure gradient ( $\nabla P$ ); and (d) MRF ..... 39
- Fig. 4.20 Calculation results showing the steady state after foam flooding (strong foams injected;  $q_t = 1.33 \times 10^{-5} \text{ m}^3/\text{s}$  and  $f_g = 0.95$ ) at different systems: (a) total injection velocity ( $u_t$ ,  $\text{m/s}$ ); (b) water saturation ( $S_w$ ); (c) pressure gradient ( $\nabla P$ ); and (d) MRF..... 40



Fig. 4.21 A schematic showing the transition from strong-foam to weak-foam state at the threshold velocity of $u_{sf}$ and threshold distance of $r_{sf}$ .....	42
Fig. 4.22 Three different injection foam qualities to test foam characteristics in field-scale applications: (a) contour map showing injection conditions; and (b) contour map showing the positions corresponding to $r_{sf}$ .....	44
Fig. 4.23 Pressure and MRF profile along the reservoir at $f_g = 0.80$ .....	45
Fig. 4.24 Pressure and MRF profile along the reservoir at $f_g = 0.95$ .....	45
Fig. 4.25 Pressure and MRF profile along the reservoir at $f_g = 0.875$ .....	45
Fig. 4.26(a) Pressure and MRF profile along the reservoir at $f_g = 0.80$ (grid block size 0.2 ft rather than 2 ft) .....	47
Fig. 4.26(b) Pressure and MRF profile along the reservoir at $f_g = 0.95$ (grid block size 0.2 ft rather than 2 ft) .....	47
Fig. 4.26(c) Pressure and MRF profile along the reservoir at $f_g = 0.875$ (grid block size 0.2 ft rather than 2 ft) .....	47
Fig. 4.27 The distance for strong foams to travel before turning into weak foams ( $r_{sf}$ ) as a function of foam quality ( $f_g$ ) and injection rates ( $q_t$ ).....	48
Fig. 4.28 Pressure profile comparing mechanistic model and constant-MRF model: (a) strong foams in the low-quality regime ( $f_g = 0.80$ ) and (b) strong foams in the high-quality regime ( $f_g = 0.95$ ) .....	49
Fig. 4.29 Foam propagation at fixed injection pressure and foam quality ( $f_g = 0.80$ , $r_w = 5$ in , $r_e = 330$ ft , $P_{out} = 2000$ psia): (a) pressure profile at various inlet pressure (2060 to 8660 psia) and (b) the distance for strong foams to travel before turning into weak foams ( $r_{sf}$ ).....	50
Fig. 4.30 Foam propagation at fixed injection pressure and foam quality ( $f_g = 0.95$ , $r_w = 5$ in , $r_e = 330$ ft , $P_{out} = 2000$ psia): (a) pressure profile at various injection pressure (2020 to 7700 psia) and (b) distance for strong foams to travel before turning into weak foams ( $r_{sf}$ ) vs. injection pressure .....	51

## **ABSTRACT**

A numerous laboratory and field tests revealed that foam can effectively control gas mobility, improve sweep efficiency, and increase oil production, if correctly designed. It is believed that there is a significant gap between small laboratory-scale experiments and large field-scale tests because of two main reasons: (i) typical laboratory flow tests are conducted in linear systems, while field-scale foam EOR processes are performed in radial (or spherical partly) systems in general; and (ii) through the complicated in-situ lamella creation and coalescence mechanisms and non-Newtonian behavior, foam rheology is thought to depend on geometry and dimensionality and, as a result, it is often not clear how to translate laboratory-measured data to field-scale applications.

Therefore, this study for the first time investigates how foam rheological properties change in different dimensions and geometries and how such dimensionality-dependent properties are affected by different foam flowing conditions by using mechanistic foam fractional flow analysis. Complex foam characteristics such as three foam states (weak-foam, strong-foam, and intermediate state; sometimes referred to as foam catastrophe theory) and two steady-state strong-foam regimes (high-quality regime and low-quality regime) lie in the heart of this analysis.

The calculation results from a small radial or spherical system showed that (i) for strong foams in the low-quality regime injected, foam mobility decreased (or mobility reduction factor increased) significantly with distance which improved sweep efficiency; (ii) for strong foams in the high-quality regime, the situation became more complicated – near the well foam mobility decreased, but away from the well foam mobility increased with distance, which eventually gave lower sweep efficiency; and (iii) for weak foams injected, foam mobility increased with distance

which lowered sweep efficiency. The results also implied that the use of fixed value of mobility reduction factor, which is common practice in reservoir simulations, might lead to a significant error, especially for strong foams in the low-quality regime. When the method was applied to the large field-scale applications, it was first shown why strong foams would eventually turn into weak foams. Then additional results showed that strong foams could propagate deeper into the reservoir at higher injection rate, higher injection pressure, and at lower injection foam quality. Foam propagation distance was very sensitive to these injection conditions for foams in the high-quality regime, but much less sensitive for foams in the low-quality regime.

This study uses a mechanistic foam model similar to Afsharpoor et al. (2010) which is an updated version of Kam and Rossen (2003), Kam et al. (2007), and Kam (2008). In all calculations, gas and liquid phases are assumed to be incompressible and the presence of oil is not considered at this stage.

## CHAPTER 1. INTRODUCTION

### 1.1 Background of This Study

Even though foam has been applied into many pilot-scale and reservoir-scale EOR processes successfully (see examples in Siggins field, Illinois (Holm, 1970); Dome-Tumbador, Midway-Sunset field, California (Mohammadi et al., 1989); 26C, Midway-Sunset field, California (Friedmann et al., 1994); SACROC field, Texas (Sanders et al., 2012); EVGSAU field, New Mexico (Harpole et al., 1994); Tapis field, Malaysia (Wan-Mohamad et al., 2005) and so on), how foam propagates in a large multi-dimensional scale still remains unclear. It is because the high pressure gradient, often needed to create fine-textured strong foams in 1D coreflood experiments, does not happen easily in multi-dimensional spaces such as radial and spherical geometries.

Although limited, there exist experimental studies which investigated how foam behaves in a system where the cross-sectional area changes. Friedmann et al. (1994) claimed from their 2-ft-long cone-shaped (3D) Ottawa sandpack foam flood experiments that strong foams, first created near the injection well where the pressure gradient is relatively high due to small cross-sectional area, may propagate deep into the reservoir towards production wells. By conducting foam flood experiments in a 1-ft long 1D sandpack column and in a 2 ft x 2 ft x 2.5 ft (height) sandpack, Li et al. (2006) showed that the resistance during foam flow in a 3D spherical geometry is about 5 times less than that in a 1D linear geometry. Kovscek et al. (1997) simulated foam propagation into 1-m thick, 71.5 m radius, and 1.3 darcy radial homogeneous porous medium. They confirmed fine texture close to the injector but falls off quickly with foam movements.

## **1.2 Motivation and Objectives of This Study**

Even with these pioneering studies, fundamentals of dimensionality-dependent foam behaviors seem not understood well. This is why planning and design of field-scale foam EOR processes, where the cross-sectional area changes drastically in radial or spherical geometries, have been a major challenge.

Therefore, the objective of this study is to investigate the dimensionality-dependent or geometry-dependent foam rheology where the total velocity decreases as foam moves into the system by using mechanistic foam modeling technique. It is assumed at this stage that there is no oil present in the system and phases are incompressible.

## **1.3 Chapter Description**

This study consists of five main chapters as follows:

Chapter 1 introduces the background, motivation, and objectives of this study.

Chapter 2 covers the fundamentals of foam flow in porous media, which are the foundation of this study, as well as recent advances in foam research including three different foam states relevant to foam catastrophe theory and two steady-state strong-foam regimes.

Chapter 3 describes mathematical background for the mechanistic modeling techniques implemented in this study and the system of interest to be investigated in this study.

Chapter 4 presents details of research outcomes with discussions, first foam propagation in small systems to examine fundamental behaviors of foam characteristics and second the implication of such results in large field-scale applications.

Chapter 5 summarizes this study with conclusions and future research topics.

## **CHAPTER 2. LITERATURE REVIEW**

### **2.1 Introduction of Foams**

Although gas injection is popular to enhance oil recovery from petroleum reservoirs, its efficiency is significantly diminished because gas phase tends to flow through high-permeability layers (channeling), segregate from liquid phase (gravity segregation), and finger through low-mobility fluids ahead (viscous fingering) (Lake, 1989). These aspects make it difficult for the injected gas to invade zones with high oil saturations in field applications. Foaming the gas phase to mitigate these problems has been recognized as a potentially promising solution even in early days as shown by Bond and Holbrook (1958) in their experiments with glass tubes filled with sands and Bernard and Holm (1964) in their experiments with Berea sandstone cores.

The effectiveness of foam application to improve sweep efficiency and oil recovery has been proved through field pilot tests since 1970. For example, Holm (1970) showed from foam pilot tests in Siggins field in Illinois that by injecting 0.02 PV and 0.06 PV of 1 percent foaming agent into the formation, both water mobility and gas mobility were reduced more than 50 % and 70 % respectively, resulting in a large reduction in water production. Mohammadi et al. (1989) presented a field pilot test in Dome-Tumbador, Midway-Sunset field, California that by injecting continuous steam foams for two years, 207,000 bbl of incremental oil was produced. Friedmann et al. (1994) also showed a foam field trial in Section 26C of the Midway-Sunset field. Over one and half year of steam-foam injection, a substantial improvement in vertical and areal sweep of the reservoir was observed and 27,000 bbl of incremental oil was produced. In order to propagate deep into the reservoir, foam should not only be created in-situ as it travels, but should also resist to the possible disturbances causing instability.

A reduction in gas mobility during foam flow has also been observed in laboratory experiments. For example, Falls et al. (1988), conducting flow experiments by using pre-generated foams and glass tubes (internal diameters of 1.4, 1.1, and 0.95 cm, length of 60 cm; filled with equal-size glass beads (0.23 and 0.3 cm in diameter)), concluded that foams with both low and high viscosities can reduce gas mobility by affecting relative permeability and apparent gas viscosity.

Ransohoff et al. (1988) investigated mechanisms of creation of foam films in porous media (often referred to as lamella creation) in a 6 x 25 x 165 mm glass bead pack filled with beads, mostly diameters of 1 mm or smaller. Their study visually identified three different in-situ lamella creation mechanisms: lamella leave-behind, gas-bubble snap-off, and lamella division as illustrated in Fig. 2.1.

Lamella leave-behind mechanism occurs when gas phase passes through the liquid-filled pores during drainage process. The injected gas phase “leaves” liquid collars “behind” at the adjacent pore throats in the direction parallel to the flow. These liquid collars, unstable in the absence of surfactant, can thin out and form lamellae.

Snap-off mechanism occurs when there is enough fluctuation in capillary pressure ( $P_c$ ) as non-wetting gas phase intrudes into the liquid-filled pores. During this event, the capillary pressure at the leading edge of gas-water interface first rises above capillary entry pressure ( $P_c^e$ ) as the interface passes through the pore throat, and then subsequently the capillary pressure falls below a capillary pressure value required for snap-off, so-called snap-off capillary pressure ( $P_c^{sn}$ ).  $P_c^{sn}$  is shown to be geometry-dependent and about a half of  $P_c^e$  in converging-and-diverging conical pore geometry (Fall et al., 1988).

Lamella division mechanism (or, often called lamella mobilization-and-division mechanism in full), first requires a pre-existing lamella which can subsequently be mobilized by a sufficient pressure gradient called the minimum pressure gradient for mobilization ( $\nabla P_{\min}$ ). The mobilized lamella can be multiplied at the downstream junctions.

Snap-off is regarded as a major lamella-creation mechanism in heterogeneous media where the average pore sizes change dramatically, while lamella division is regarded as a major mechanism in homogeneous media (Gauglitz et al, 2002; Kam and Rossen, 2003).

On the other hand, lamella coalescence is governed by disjoining pressure ( $\Pi$ ) (or, capillary pressure, equivalently) - lamella thins down and breaks down if the situation exceeds the maximum value of disjoining pressure ( $\Pi_{\max}$ ), so-called limiting capillary pressure ( $P_c^*$ ), which is an outcome of combining electrostatic repulsive and Van der Waals attractive forces shown in Fig. 2.2 (Miller and Neogi, 1985). Note that this  $\Pi_{\max}$  or  $P_c^*$  corresponds to a threshold value of foam film thickness ( $h_{cr}$ ) below which the film cannot sustain. For a population of bubbles in porous media, this concept of  $P_c^*$  is also valid, and the use of  $P_c^*$  to evaluate the stability of lamellae can be translated well in terms of limiting water saturation ( $S_w^*$ ). For example,  $P_c < P_c^*$ , the condition for existing foams to be stable, is equivalent to  $S_w > S_w^*$  because capillary pressure is related to water saturation. Once in motion along the pores, lamellae tend to be stretched out and may break if the transport of aqueous phase does not take place quickly enough (Jimenez and Radke, 1996).



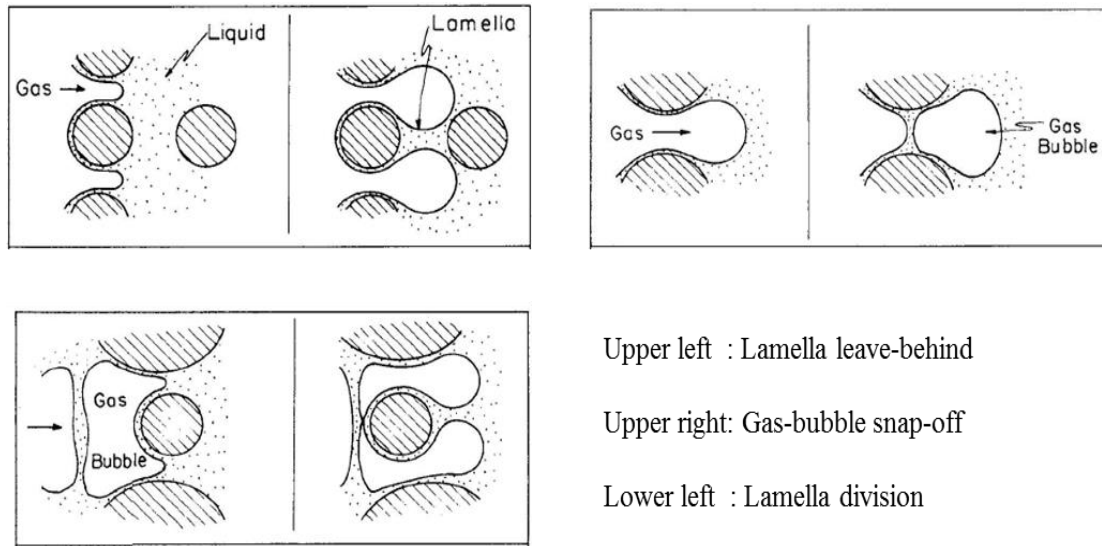


Fig. 2.1 Three in-situ lamella-creation mechanisms (from Ransohoff et al. (1988))

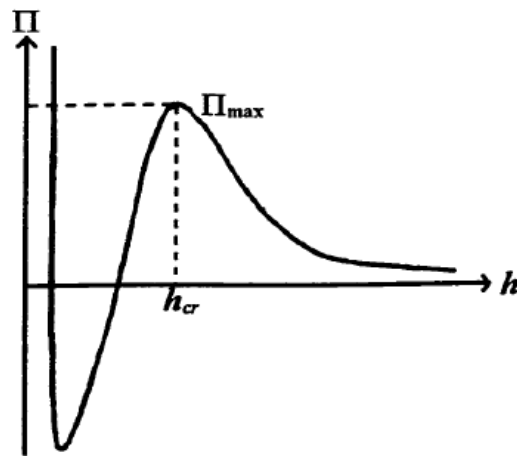


Fig. 2.2 Disjoining pressure curve ( $\Pi$ ) as a function of foam film thickness ( $h$ ), demonstrating minimum film thickness for stability ( $h_{cr}$ ) and corresponding maximum disjoining pressure ( $\Pi_{max}$ ) (from Miller and Neogi (1985))

Foam texture, or the number of lamellae in unit volume, is a resulting outcome of these various mechanisms of lamella creation and coalescence within porous media. Based on how foam texture is determined, there exist largely two different foam modeling techniques in the literature. A technique called “local-steady-state” modeling uses pre-determined steady-state foam mobility or a factor which compares foam mobility to gas-phase mobility (so-called mobility reduction factor). This mobility reduction factor (MRF) depends on various experimental conditions including surfactant concentration, oil and water saturations, and capillary number and so on (Ma et al., 2013). Another technique called “bubble-population-balance” modeling uses foam texture as a function of rates of lamella creation and coalescence in situ which vary in space and time, and foam mobility is determined accordingly in response to foam texture and other foam properties (Falls et al., 1988; Friedmann et al., 1991; Kovscek et al., 1995).

A fine-textured foam exhibiting low water saturation and high gas viscosity (or, high pressure gradient equivalently), so-called “strong foam”, can be obtained if the rate of lamella creation prevails the rate of lamella coalescence. On the other hand, a coarse-textured foam exhibiting high water saturation and low gas viscosity (or, low pressure gradient equivalently), so-called “weak foam”, can be obtained if the rate of lamella coalescence prevails the rate of lamella creation (Falls et al., 1988; Friedmann et al., 1991). A sudden and abrupt shift from weak foam to strong foam, accompanied by a significant increase in pressure gradient (often as much as a few orders of magnitude), is called “foam generation”.

Foam quality, representing a volume fraction of gas phase in the whole gas and liquid (surfactant solution) mixture, is another important parameter to describe foam properties. For

example, foam quality of 80% (or 0.8 in terms of fraction) means that the mixture consists of 80% gas and 20% liquid.

## **2.2 Recent Developments: “two steady-state foam-flow regimes” and “three foam states”**

When it comes to foam rheological properties in porous media, two recent findings such as “two steady-state foam-flow regimes” and “three foam states” should be highlighted and are thus used as a basis for this study.

If strong foams are created through the process called foam generation, they are shown to exhibit two distinct foam-flow regimes so called high-quality regime and low-quality regime as shown by pressure contours as functions of gas and liquid velocities in Fig. 2.3 (Osterloh and Jante, 1992), where those two regimes are divided by a threshold value of foam quality called  $f_g^*$ . Note that, in the high-quality regime, the steady-state pressure gradient is primarily dependent upon liquid velocity and very insensitive to gas velocity due to almost vertical pressure contours, while the opposite happens in the low-quality regime. Foam rheology is typically near-Newtonian or slightly shear-thickening in the high-quality regime, but highly shear-thinning in the low-quality regime. These two regimes are shown to be governed by different mechanisms such as limiting capillary pressure in the high-quality regime and bubble trapping and mobilization in the low-quality regime (Alvarez et al., 2001; Rossen and Wang, 1999). Note that the curve representing  $f_g^*$  tends to be concave due to different foam rheological properties in the two regimes. More in-depth discussions about these two flow regime concept are thoroughly given in Alvarez et al. (2001).

By conducting foam coreflood experiments with three different types of constraints (controlling the pressure drop, flow rates, or a combination of both) in a wide range of

experimental conditions, Gauglitz et al. (2002) presented a new way of describing the process of foam generation in a three-dimensional space as shown in Fig. 2.4: a strong-foam state represented by the top surface, a weak-foam state represented by the bottom surface, and an intermediate state connecting those two surfaces in between. Their study experimentally confirmed that an injection condition with fixed injection gas and liquid rates may have multiple solutions while an injection condition with fixed injection pressure is guaranteed to have a single solution. This means that a slice of the surface in a vertical direction leads to an S-shaped curve, as represented by Fig. 2.5, consisting of the three foam states. The presence of such an S-shaped foam-generation surface, later referred to as foam catastrophe theory (Kam and Rossen, 2003; Kam 2008), implies that lamella mobilization and division is the main lamella creation mechanism in homogeneous porous media.

Based on the earlier versions of bubble population foam modeling and simulation (Friedmann et al., 1991; Falls et al., 1988; Kovscek et al., 1995), Kam and Rossen (2003) proposed a new population balance model that incorporated the concept of minimum pressure gradient for mobilization. Their results successfully reproduced three different foam states and two steady-state strong foam regimes as shown in Figs. 2.5 (solids line) and 2.6. An extension of Kam and Rossen' model can be found in the follow-up studies to improve foam simulations in the low-quality regime (Kam et al., 2007), in the high-quality regime (Kam, 2008), and in the process of gas-liquid co-injection (Afsharpoor et al., 2010).

In addition, such a foam rheological model can be combined with fractional flow analysis (referred to as mechanistic foam fractional flow analysis) in order to understand velocity-

dependent fractional flow curves and displacement efficiency (Dholkawala et al., 2007; Ashoori et al., 2012).

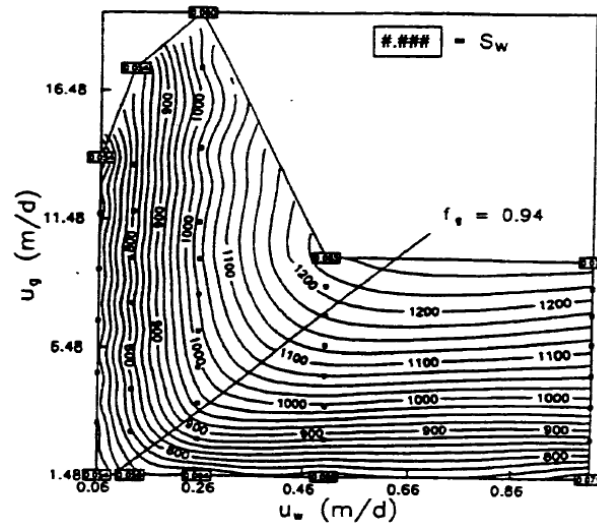


Fig. 2.3 A contour map showing two distinct foam flow regimes obtained from laboratory flow experiments (from Osterloh and Jante (1992))

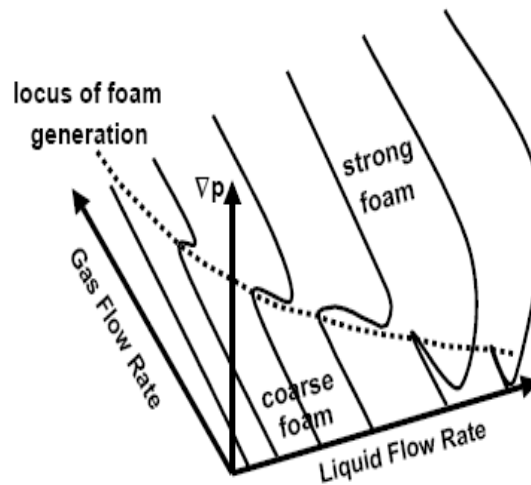


Fig. 2.4 A schematic figure showing three different foam states such as weak-foam (or coarse-foam), strong-foam and intermediate states (from Gauglitz et al. (2002))

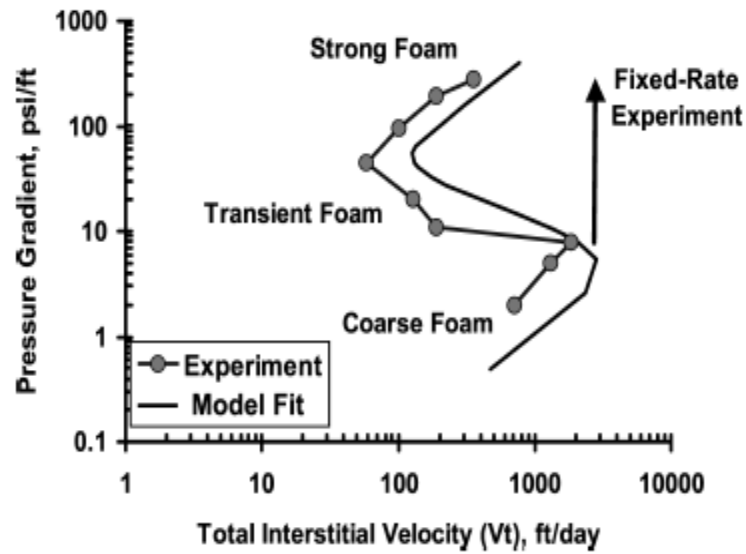


Fig. 2.5 An S-shaped foam-generation curve showing three different foam states (from Kam and Rossen (2003))

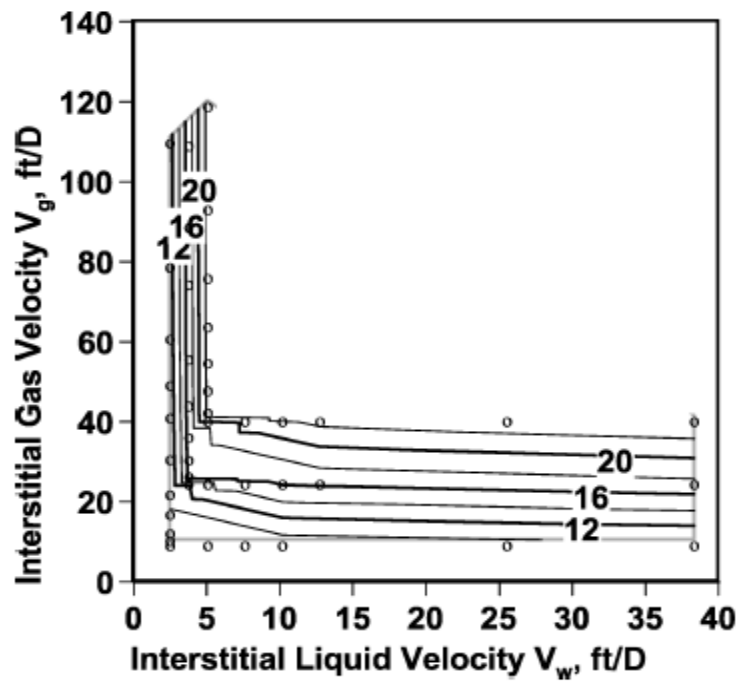


Fig. 2.6 A contour map showing two steady-state strong-foam regimes reconstructed by Kam and Rossen (2003) by using mobilization pressure gradient concept

## CHAPTER 3. METHODOLOGY

### 3.1 Mechanistic foam model and model parameters

By and large, this study uses the mechanistic bubble-population-balance model of Afsharpoor et al. (2010) as a basis, combined with mass balance equation. The mass balance with assumptions of no absorption and no mass transfer between two immiscible phases is given by Buckley and Leverett (1942), i.e.,

$$\frac{\partial}{\partial t}(\phi \rho_j S_j) + \nabla \cdot (\rho_j \vec{u}_j) = G, \quad j = w \text{ or } g \quad (3.1)$$

where  $\phi$  is porosity,  $t$  is time, and  $\rho_j, S_j$ , and  $u_j$  are the density, saturation, and superficial velocity of phase  $j$  ( $j = w$  for water, and  $j = g$  for gas) respectively. Note that the superficial velocity ( $u_j$ ) is no other than flow rate ( $q_j$ ) over a cross-sectional area ( $A$ ) (i.e.,  $u_j = q_j/A$ ). For one-dimensional incompressible flow without a sink or source term ( $G$ ) at fixed total injection velocity ( $u_t$ ), Eq. (3.1) can be simplified to an equation commonly called fractional flow equation in one-dimensional space, that is,

$$\frac{\partial}{\partial t}(S_j) + \frac{u_t}{\phi} \frac{\partial}{\partial x}(f_j) = 0, \quad j = w \text{ or } g \quad (3.2)$$

Note that porosity  $\phi$  is assumed to be uniform and constant irrespective of location ( $x$ ) and time ( $t$ ), and  $u_t$  is the sum of gas superficial velocity ( $u_g$ ) and liquid superficial velocity ( $u_w$ ). The fractional flow of water ( $f_w$ ) in horizontal flow direction with negligible capillary pressure gradient is expressed by

$$f_w = 1 - f_g = \frac{u_w}{u_t} = \frac{u_w}{u_w + u_g} = \left(1 + \frac{k_{rg}(S_w)/\mu_g}{k_{rw}(S_w)/\mu_w}\right)^{-1} \quad (3.3)$$

where  $\mu_j$  and  $k_{rj}$  are viscosity and relative permeability of phase  $j$ .

Bubble population balance in the gas phase is obtained in a similar way (Falls et al., 1988; Freidmann et al., 1991; Kovscek et al., 1995), i.e.,

$$\emptyset \frac{\partial}{\partial t} (S_g n_f) + \frac{\partial}{\partial x} (n_f u_g) = \emptyset S_g R \quad (3.4)$$

where  $n_f$  is foam texture (or, bubble population density, equivalently) and  $R$  is the net rate of bubble population change in time. The net rate ( $R$ ) is a combination of the rate of lamella creation ( $R_g$ ) and the rate of lamella coalescence ( $R_c$ ), i.e.,

$$R = R_g - R_c \quad \text{if } S_w > S_w^* \quad (3.5)$$

Notice that if  $S_w$  is less than or equal to the limiting water saturation ( $S_w^*$ ), the net rate is zero and no foam film exists.  $R_g$  and  $R_c$  are defined as

$$R_g = \frac{C_g}{2} \left[ \operatorname{erf} \left( \frac{\nabla P + \nabla P_0}{\sqrt{2}} \right) - \operatorname{erf} \left( \frac{-\nabla P_0}{\sqrt{2}} \right) \right] \quad \text{and} \quad (3.6)$$

$$R_c = C_c n_f \left( \frac{S_w}{S_w - S_w^*} \right)^n \quad \text{if } S_w > S_w^* \quad (3.7)$$

where  $C_g$  and  $\nabla P_0$  are two model parameters required for lamella creation,  $C_c$  and  $n$  are two model parameters required for lamella coalescence, and  $\operatorname{erf}$  is the error function (Acton, 1990).  $\nabla P_0$  is related to the minimum pressure gradient for lamella mobilization and division (Rossen and Gauglitz, 1990; Kam and Rossen, 2003). According to Kam (2008) and Afsharpoor et al. (2010), these  $R_g$  and  $R_c$  functions are expected to capture the change in bubble population in homogeneous media as illustrated by Fig. 3.1:  $R_g$  increases and accelerates with  $\nabla P_0$  at low pressure gradient;  $R_g$  decelerates and levels off with  $\nabla P_0$  at high pressure gradient; and  $R_c$  increases dramatically as  $S_w$  approaches down to  $S_w^*$ .



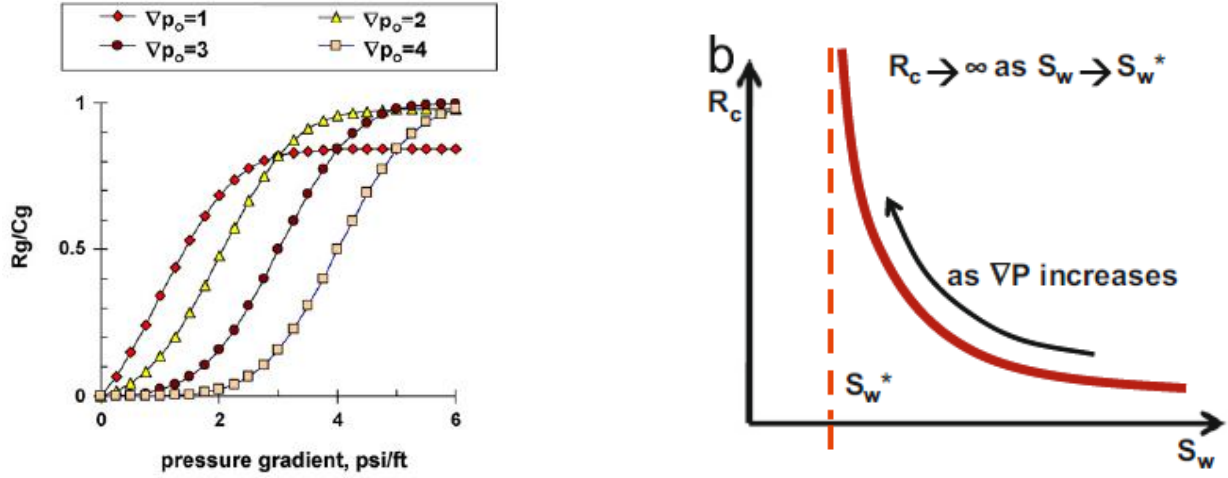


Fig. 3.1 The rate of lamella creation (from Kam, 2008) and the rate of lamella coalescence (from Afsharpoor et al., 2010) used in this study

Foam texture ( $n_f$ ) at local steady state can be determined by making  $R_g$  and  $R_c$  equal to each other, therefore,

$$n_f = \frac{C_g}{2C_c} \left( \frac{S_w}{S_w - S_w^*} \right)^n \left[ \text{erf} \left( \frac{\nabla p + \nabla p_0}{\sqrt{2}} \right) - \text{erf} \left( \frac{-\nabla p_0}{\sqrt{2}} \right) \right] \text{ if } n_f < n_{fmax} \quad (3.8)$$

where  $n_{fmax}$  is the maximum foam texture (corresponding to the maximum number of foam films in unit volume) that is related to the minimum bubble size. Note that the bubble size cannot be smaller than average pore size due to diffusion (Rossen and Wang, 1999).

A significant amount of gas saturation is shown to be trapped during foam flow (Friedmann et al., 1991; Kovscek and Radke, 1994). Such a concept can be described by using flowing gas saturation ( $S_{gf}$ ) and trapped gas saturation ( $S_{gt}$ ). The fraction of trapped gas saturation ( $X_t$ ) from Kovscek et al. (1995), which suggests use of an expression similar to Langmuir isotherm, is employed in this study, i.e.,

$$X_t = X_{tmax} \left( \frac{\beta n_f}{1 + \beta n_f} \right) \quad (3.9)$$

where  $X_{\text{tmax}}$  is the maximum fraction of trapped gas saturation, typically ranging from 0.70 to 0.95, and  $\beta$  is a parameter defining how quickly the equilibrium state is obtained. Note that the fraction of flowing gas saturation ( $X_f$ ) is simply  $1 - X_t$ . Gas saturation is related to these parameters as follows:

$$S_g = S_{gt} + S_{gf} \quad \text{and} \quad (3.10)$$

$$S_g = X_t S_g + X_f S_g = X_t S_g + (1 - X_t) S_g \quad (3.11)$$

Because the presence of foam does not affect liquid relative permeability function (Friedmann et al., 1991; Kovscek et al., 1995), Darcy's equation for liquid velocity ( $u_w$ ) and gas velocity ( $u_g$ ) can be expressed as follows:

$$u_w = \frac{kk_{rw}^f(S_w)}{\mu_w} \nabla P, \quad (3.12)$$

$$u_g = \frac{kk_{rg}^o(S_w)}{\mu_g^o} \nabla P, \quad \text{and} \quad (3.13)$$

$$u_g = \frac{kk_{rg}^f(S_w)}{\mu_g^f} \nabla P \quad (3.14)$$

where superscript "o" and "f" represents a condition without foam and with foam. The effective foam viscosity ( $\mu_g^f$ ) is given by Hirasaki and Lawson (1985), i.e.,

$$\mu_g^f = \mu_g^o + \frac{C_f n_f}{\{u_g / (\phi S_g X_f)\}^{1/3}} \quad (3.15)$$

where  $C_f$  is a model parameter accounting for the resistance exerted by foams. Liquid relative permeability ( $k_{rw}$ ), gas relative permeability without foam ( $\mu_g^o$ ), and gas relative permeability with foam ( $\mu_g^f$ ) for the model used in this study are given as follows:

$$k_{rw} = 0.7888 \left( \frac{S_w - S_{wc}}{1 - S_{wc} - S_{gr}} \right)^{1.9575} \quad (3.16)$$

$$k_{rg}^o = \left( \frac{1 - S_w - S_{gr}}{1 - S_{wc} - S_{gr}} \right)^{2.2868} \quad (3.17)$$

$$k_{rg}^f = \left( X_f \frac{1 - S_w - S_{gr}}{1 - S_{wc} - S_{gr}} \right)^{2.2868} \quad (3.18)$$

where  $S_{wc}$  and  $S_{gr}$  are connate water saturation and residual gas saturation.

A reduction in gas mobility in the presence of foam is sometimes expressed by using mobility reduction factor (MRF). If so, the fractional flow of liquid phase in Eq. (3.3) can be modified to be

$$f_w = \left( 1 + \frac{k_{rg}^o(S_w)/(\mu_g^o MRF)}{k_{rw}(S_w)/\mu_w} \right)^{-1} \quad (3.19)$$

If  $MRF = 1$ , no foam is present, and this equation becomes conventional fractional flow equation for gas-water two phases. If  $MRF > 1$ , gas mobility is reduced by foam and it leads to a reduction in water saturation. Eq. (3.19) can be rewritten for MRF as follows by using Eqs. (3.13) and (3.14):

$$MRF = \frac{k_{rg}^o(S_w)\mu_g^f}{k_{rg}^f(S_w)\mu_g^o} \quad (3.20)$$

As a recap, there are nine parameters for the foam mechanistic model used in this study:  $C_g$  and  $\nabla P_0$  are parameters for lamella creation,  $C_c$ ,  $n$ , and  $S_w^*$  for lamella coalescence,  $C_f$  for apparent foam viscosity,  $X_{tmax}$  and  $\beta$  for trapped gas saturation and  $n_{fmax}$  for average pore size and minimum bubble size. These parameters can be obtained by fitting experimental data showing two strong-foam flow regimes, three foam states, and gas trapping.

### 3.2 Discretization of the system

This study first considers how foam rheology changes as it propagates in a radial geometry and then extends the same logic to a spherical geometry – the first being a typical reservoir shape in field EOR operations and the second being a typical flow pattern before the reservoir top and bottom boundaries are felt.

Fig. 3.2 shows how a system with radial geometry is defined and how such a system is discretized in this study as an example. The system, initially saturated with water at its residual gas saturation  $((S_w, S_g) = (1-S_{gr}, S_{gr}))$ , has the wellbore radius of  $r_w$  and the external radius of  $r_e$ . At the inlet, both gas and water are injected at the pre-determined injection quality ( $f_g$ ) and total injection rate ( $q_t$ ), while at the outlet fluids are produced at the pre-specified backpressure ( $P_{out}$ ).

Then the total superficial velocity ( $u_t$ ) at the center of  $i$ -th segment is given by

$$u_{ti} = \frac{q_t}{2\pi h \left[ r_w + \Delta r \left( i - \frac{1}{2} \right) \right]} \quad i = 1, 2, \dots, n \quad (3.21)$$

The total superficial velocity at the inlet face ( $u_{tin}$ ) and at the outlet ( $u_{tout}$ ) are, respectively,

$$u_{tin} = \frac{q_t}{2\pi r_w h} \quad \text{and} \quad (3.22)$$

$$u_{tout} = \frac{q_t}{2\pi r_e h} \quad (3.23)$$

In case of spherical geometry, Eqs. (3.21) through (3.23) become as follows:

$$u_{ti} = \frac{q_t}{4\pi \left[ r_w + \Delta r \left( i - \frac{1}{2} \right) \right]^2} \quad i = 1, 2, \dots, n \quad (3.24)$$

$$u_{tin} = \frac{q_t}{4\pi r_w^2} \quad (3.25)$$

$$u_{tout} = \frac{q_t}{4\pi r_e^2} \quad (3.26)$$

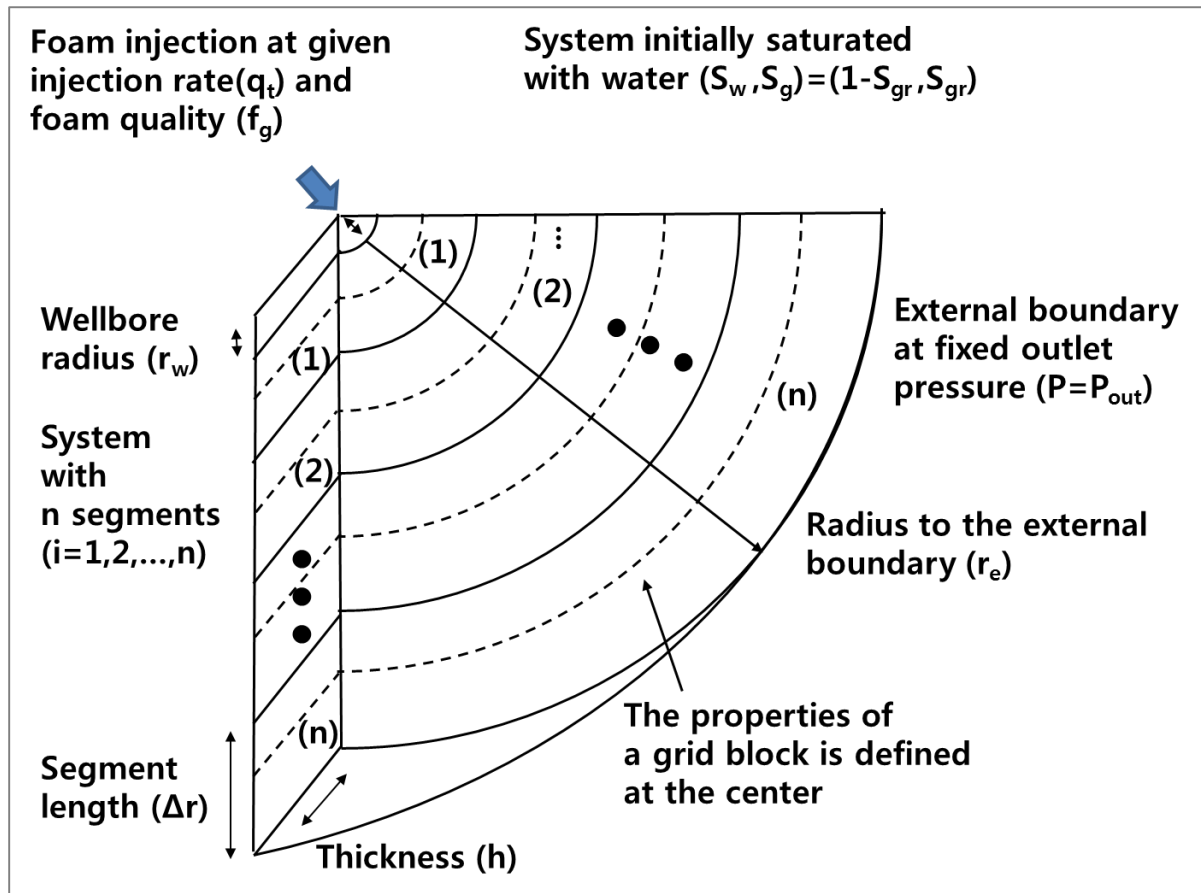


Fig. 3.2 A schematic of radial system of interest (only a quarter is shown for simplicity)  
The system can be approximated by a series of one-dimensional blocks ( $i = 1, 2, \dots, n$ ) with the segment length of  $\Delta r$  and thickness of  $h$ .

## CHAPTER 4. RESULTS AND DISCUSSIONS

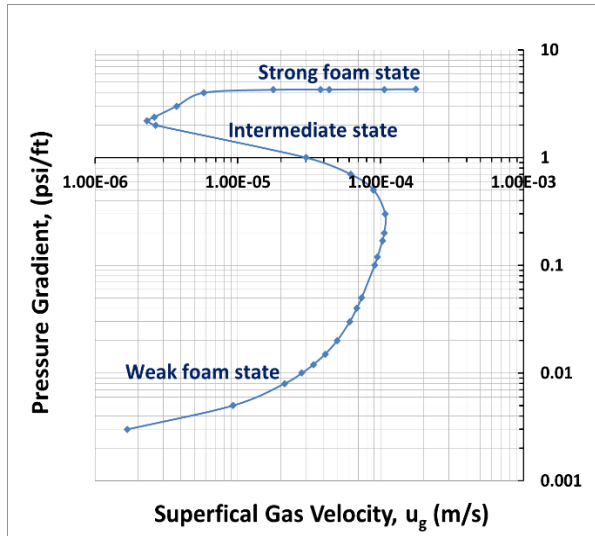
Before moving into the dimensionality-dependent foam rheological properties, an effort has been made to reproduce an S-shaped curve ( $\nabla P$  vs.  $u_g$  at fixed  $u_w$ ) and a two-flow-regime pressure-contour map. Fig. 4.1 shows the results using the basic rock and fluid properties as well as foam parameters as shown in Table 4.1, which is the same as those in Afsharpoor et al. (2010). The S-shaped curve in Fig. 4.1(a) represents a slice of the 3D surface at  $u_w = 1.0 \times 10^{-6}$  m/s. Note that  $f_g^*$  separating two flow regimes in Fig. 4.1(b) increases as  $u_t$  increases (i.e.,  $f_g$  is close to 0.80 at low velocity but goes slightly more than 0.90 at high velocity).

The model is then applied to obtain a series of S-shaped curves at different foam qualities (i.e.,  $\nabla P$  vs.  $u_t$  at fixed  $f_g$ ;  $f_g$  ranging from 0.575 to 0.99) as shown in Fig. 4.2. This plot is helpful in order to grasp the actual shape of three-dimensional foam-rheology surface and estimate foam rheology when foam is injected at a fixed injection quality. Fig. 4.3 shows the same plot but in a two-dimensional format. Within the range of  $u_t$  in this plot (roughly  $3 \times 10^{-6}$  m/s –  $4 \times 10^{-4}$  m/s),  $f_g^*$  varies around 0.80 - 0.92 (cf. Fig. 4.1). This means that the top of the S-shaped curves at  $f_g \geq 0.92$  (i.e.,  $f_g = 0.95, 0.98, \text{ and } 0.99$ ) corresponds to foam rheology of strong-foam in the high-quality regime, that at  $f_g \leq 0.80$  (i.e.,  $f_g = 0.80, 0.725, 0.65, \text{ and } 0.575$ ) corresponds to foam rheology of strong-foam in the low-quality regime, and that in between falls the transition being near  $f_g^*$  value. It is interesting to find that those curves at  $f_g \leq 0.80$  (or, strong foams in the low-quality regime) look very similar, showing the transition from one state to another taking place all at the similar locations (i.e., the transition from strong-foam state to weak-foam state at reducing  $u_t$  takes place at around  $(u_t, \nabla P) = (3.0 \times 10^{-6} \text{ m/s}, 2 \text{ psi/ft})$ ); the same transition takes place at higher  $u_t$  as  $f_g$  increases (or as the condition moves toward strong foams in the high-

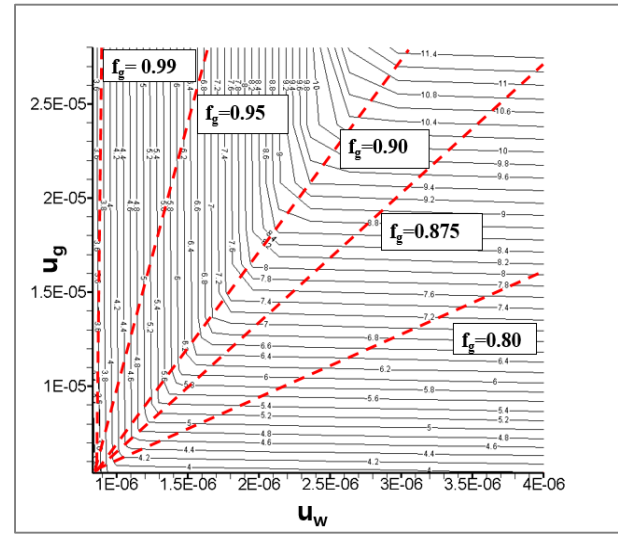
quality regime), however (e.g., the transition takes place at around  $(u_t, \nabla P) = (5.79 \times 10^{-6} \text{ m/s}, 2 \text{ psi/ft})$ ,  $(1.36 \times 10^{-5} \text{ m/s}, 2 \text{ psi/ft})$ , and  $(2.92 \times 10^{-5} \text{ m/s}, 2 \text{ psi/ft})$ , and  $(5.44 \times 10^{-5} \text{ m/s}, 2 \text{ psi/ft})$  for  $f_g = 0.875, 0.95, 0.98$ , and  $0.99$  respectively.). This tendency has an important implication when foam is applied in the field applications as discussed below (the velocity at which this transition occurs is called  $u_{tsf}$  later).

Table 4.1 Model parameters and properties used in this study (following Afsharpoor et al., 2010)

Rock properties		Basic foam properties		Foam parameters	
$k(m^2)$	$3 \times 10^{-11}$	$n_{fmax}(m^{-3})$	$8 \times 10^{13}$	$\nabla p_0(\text{psi/ft})$	4.2
$\phi$	0.3	$S_w^*$	0.0585	$n$	1.0
$\mu_w(\text{Pa s})$	0.001	$X_{tmax}$	0.8	$C_g/C_c(m^{-3})$	$3.60 \times 10^{16}$
$\mu_g^0(\text{Pa s})$	$2 \times 10^{-5}$	$\beta$	$5 \times 10^{-11}$	$C_f(\text{kg m}^{7/3} \text{s}^{-4/3})$	$6.62 \times 10^{-18}$
$S_{gr}$	0.00				
$S_{wc}$	0.04				



(a)



(b)

Fig. 4.1 Foam rheology plots reproduced by the model using model inputs in Table 4.1: (a) S-shaped curve ( $\nabla P$  vs.  $u_g$ ) at fixed  $u_w = 1.0 \times 10^{-6} \text{ m/s}$  and (b) two-flow-regime map

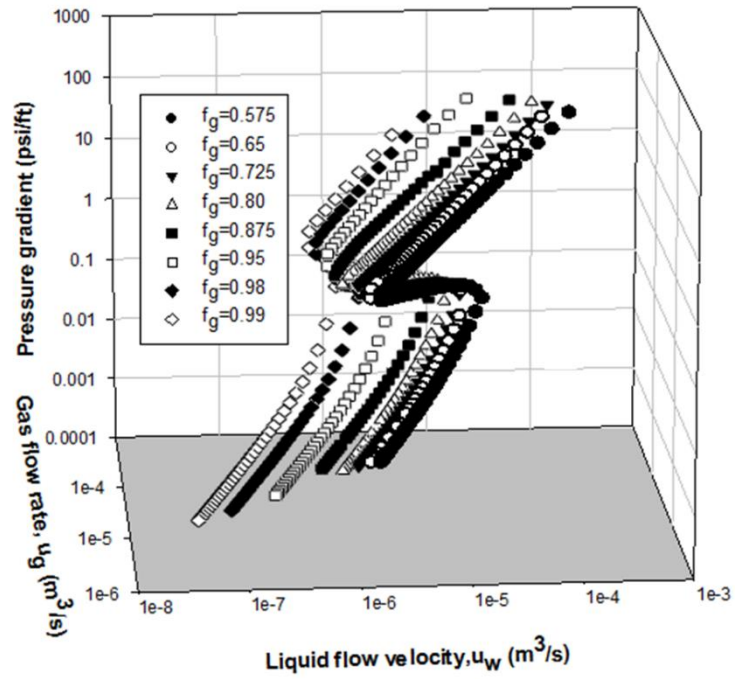


Fig. 4.2 Three-dimensional foam-rheology surface constructed by a series of S-shaped curves ( $\nabla P$  vs.  $u_t$  at fixed  $f_g$ ) at various injection foam qualities

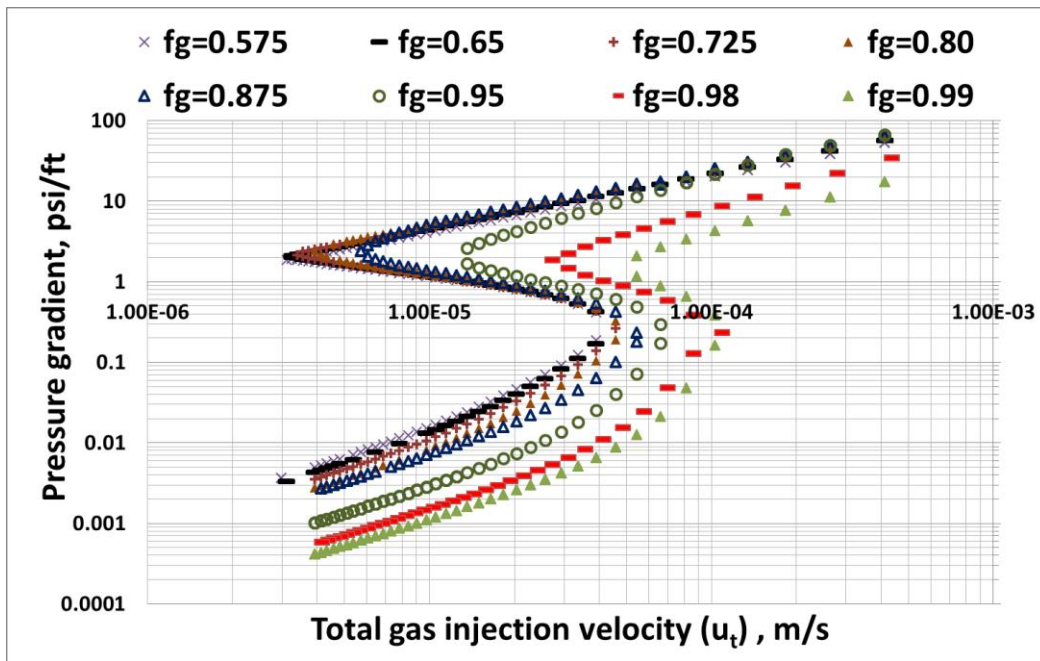


Fig. 4.3 Two-dimensional view of 3D plot shown in Fig. 4.2 ( $\nabla P$  vs.  $u_t$  at fixed  $f_g$ )



#### 4.1 Base case and its extension

As a base case, this study first investigates how foam process works in a small radial geometry. Fig. 4.4 shows the system of interest with general descriptions given in Table 4.2: a homogeneous radial system with wellbore radius ( $r_w$ ) = 2 inches, external radius ( $r_e$ ) = 14 inches, and a uniform thickness ( $h$ ) = 4 inches; foam injected at the center of the system at the total flow rate ( $q_t$ ) =  $1.33 \times 10^{-5} \text{ m}^3/\text{s}$  and injection foam quality ( $f_g$ ) = 0.80; the system initially saturated with water at its residual gas saturation ( $S_w = 1.0$  initially at  $S_g = S_{gr} = 0.0$ ). This means that a segment size ( $\Delta r$ ) of 2 inches discretizes the system with 6 grid blocks (i.e.,  $n = (r_e - r_w)/\Delta r$ ). The system length of 1 ft is selected in this modeling study because it is a typical core length used in core flood experiments.

From Eq. (3.21), the superficial velocity at the center of each grid block (i.e.,  $u_t$  values for  $i = 1$  through 6 (or,  $u_{t1}, u_{t2}, \dots, u_{t6}$ )) can be determined as shown by filled square symbols in Fig. 4.5 together with  $u_t$  values at the inlet and outlet ( $u_{tin}$  and  $u_{tout}$ ) by X symbols. The superficial velocity decreases inversely proportional to radial distance ( $r$ ) as expected. Fig. 4.6 illustrates how those  $u_t$  values can be mapped on the S-shaped curves by using the same symbols. It should be noted that because all data points fall on the top of the curve and the injection foam quality is less than  $f_g^*$ , this is the case of propagation of strong foams in the low-quality regime.

Since total velocity ( $u_t$ ) decreases with radial distance and foam rheology is velocity-dependent, it is necessary to keep track of how mechanistic foam fractional flow curves change along with radial direction. Fig. 4.7 shows mechanistic foam fractional flow curves constructed for the 6 segments representing the system. It can then be realized that the solution to foam

injection in a radial system is no other than the combination of each of those 6 solutions represented by Fig. 4.7.

Table 4.2 Description of a radial system for base-case calculation

Injection condition	Total injection flow rate ( $q_t$ ) = $1.33 \times 10^{-5} \text{ m}^3/\text{s}$ (or, 7.3 bbl/day) Fixed injection foam quality ( $f_g$ ) = 0.80
Initial condition	Fully saturated with water at residual gas saturation ( $S_{gr} = 0$ ), or $S_w = 1$
Discretized radial geometry	Thickness ( $h$ ) = 4 in Wellbore radius ( $r_w$ ) = 2 in; External radius ( $r_e$ ) = 14 in Number of segments ( $n$ ) = 6; segment size ( $\Delta r$ ) = 2 in

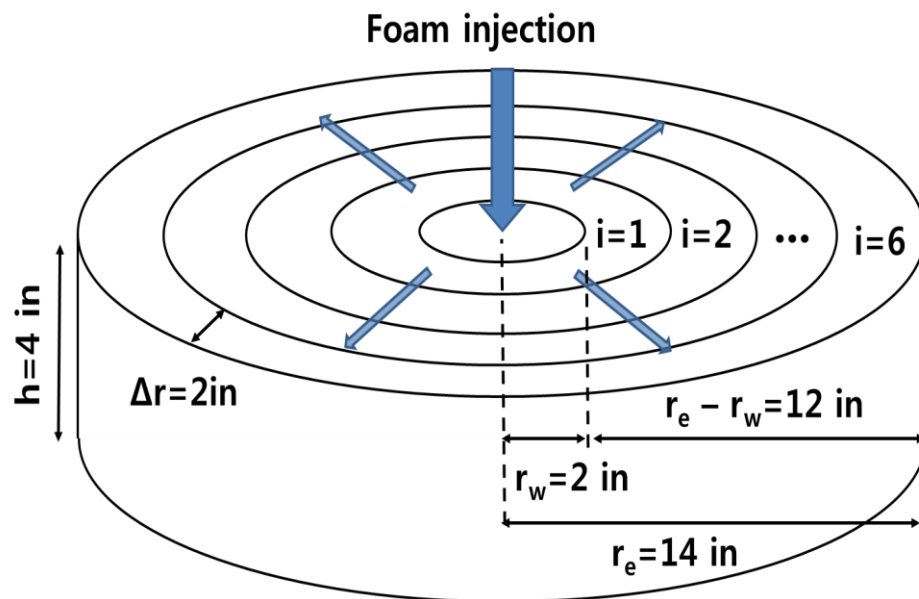


Fig. 4.4 A small-scale radial system investigated as a base case

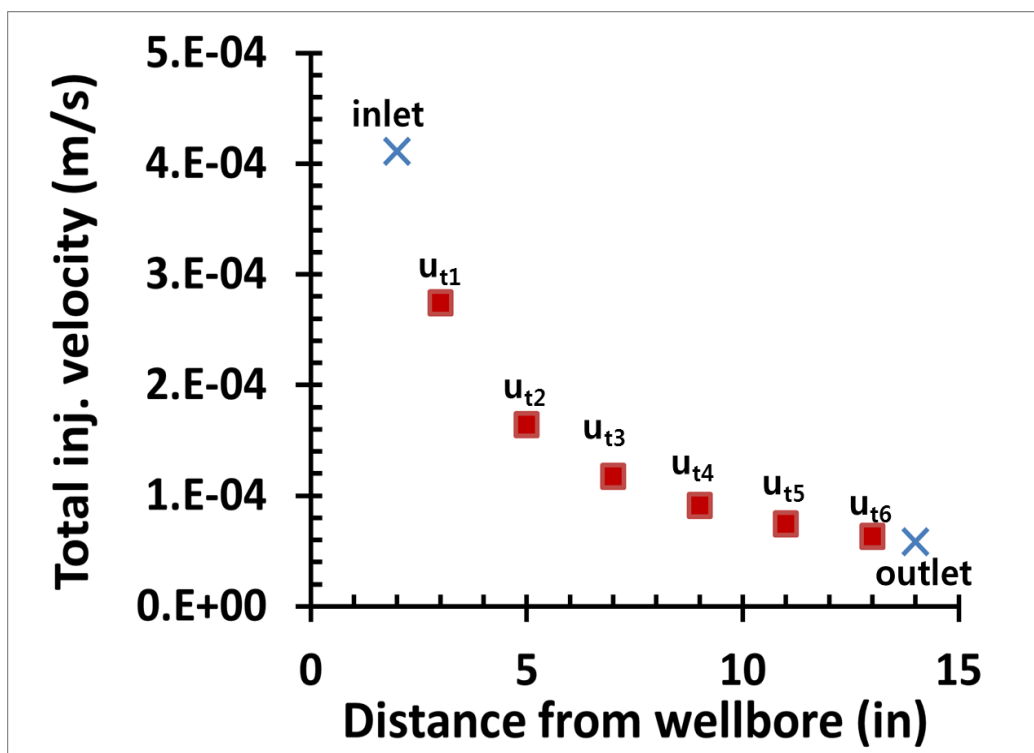


Fig. 4.5 Change in total injection velocity ( $u_t$ ) as a function of radial distance ( $r$ )

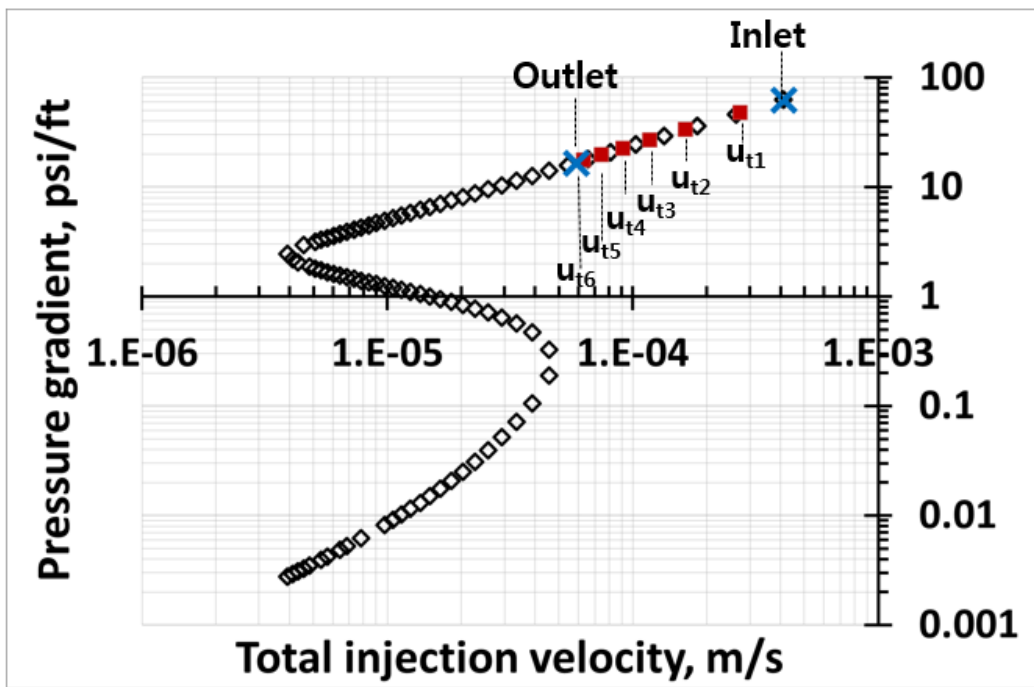


Fig. 4.6 S-shape curve at  $f_g = 0.80$  representing six segments of the base case

Once these mechanistic foam fractional flow curves are constructed, they can be used to extract mobility reduction factors (MRF) for foams in individual grid blocks (cf. Eq. (3.20)). Fig. 4.8 shows one example at  $u_t = 6.33 \times 10^{-5} \text{ m/s}$  and  $f_g = 0.80$  which represents the injection condition for the last 6<sup>th</sup> grid block. The mechanistic foam fractional flow curve is expressed by a thick solid curve with symbols, and the injection condition is given by a horizontal line. In addition, a series of fractional flow curves at different MRF values are shown. It is the MRF value of interest that intersects the mechanistic fractional flow curve at given injection condition (shown by a circle in the figure), which is about  $\text{MRF} = 10858$ . A similar procedure can be followed for other 5 grid blocks.

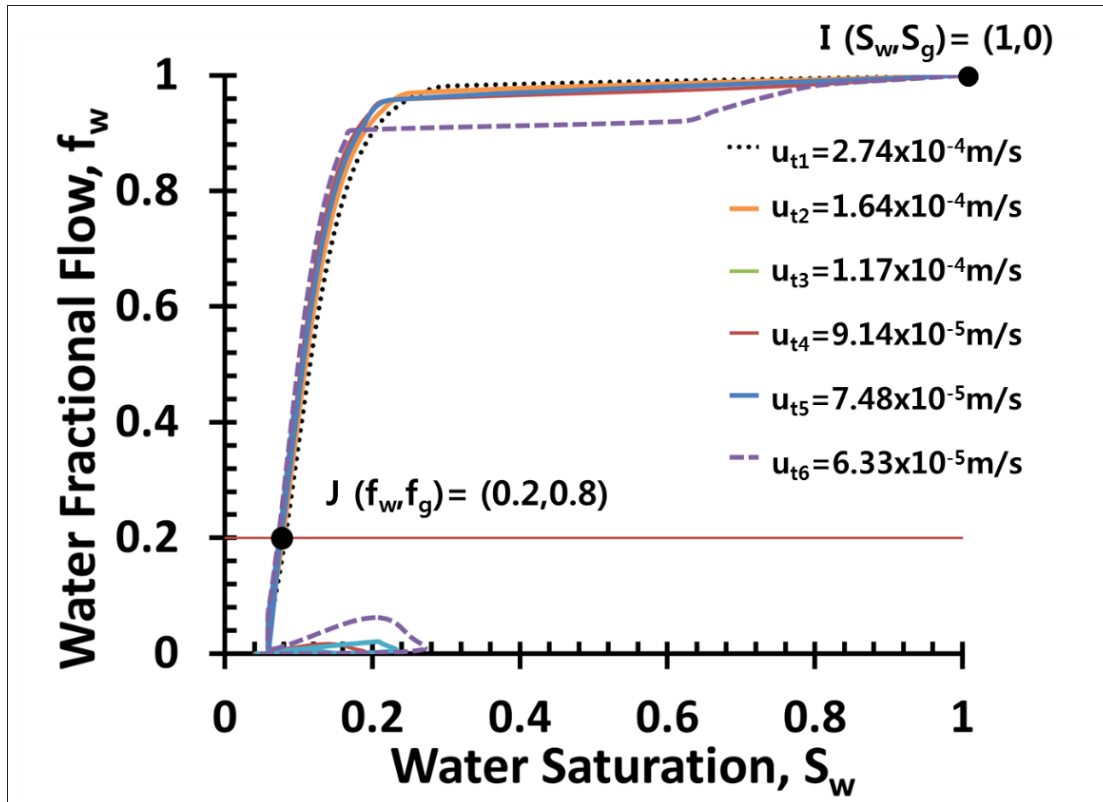


Fig. 4.7 Mechanistic foam fractional flow curves at 6 different grid blocks represented by Fig. 4.4 (total injection rate ( $q_t$ ) =  $1.33 \times 10^{-5} \text{ m}^3/\text{s}$  and injection foam quality = 0.80)

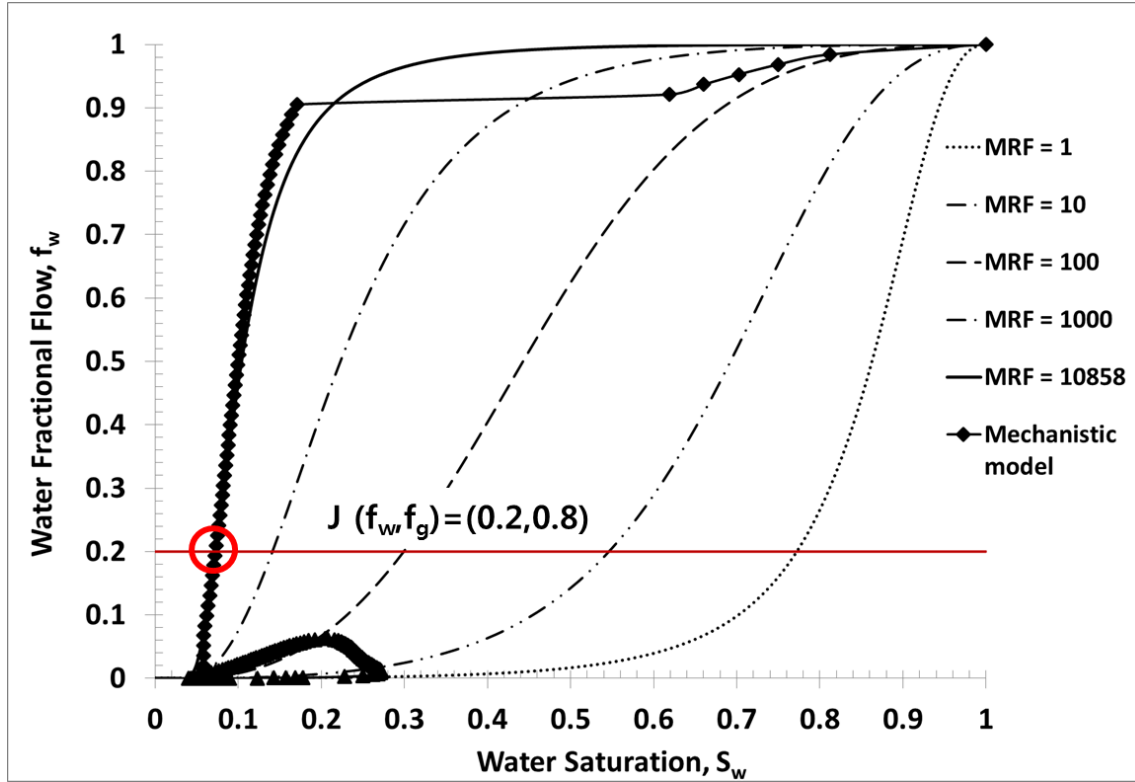


Fig. 4.8 How to find MRF values to fit foam mobility obtained by mechanistic foam fractional flow curve at  $u_t = 6.33 \times 10^{-5}$  m/s and  $f_g = 0.80$

Figs. 4.9 and 4.10 show the calculation results when the system reaches the steady state after foam sweeps the entire system (consisting of (a) water saturation ( $S_w$ ), (b) pressure ( $P$  and  $\nabla P$ ), (c) mobility ( $k_{rg}^f / \mu_g^f$ ), and (d) mobility reduction factor (MRF) for Fig. 4.9; and (a) fraction of trapped gas saturation ( $X_t$ ), (b) foam texture ( $n_f$ ), (c) gas relative permeability when foam is present ( $k_{rg}^f$ ), and (d) gas viscosity when foam is present ( $\mu_g^f$ ) for Fig. 4.10).

There are a few interesting aspects to point out for the propagation of strong foams in the low-quality regime. First, foam texture is kept at its maximum ( $n_f = n_{fmax} = 8 \times 10^{13} \text{ m}^{-3}$ ; Fig. 4.10(b)) because bubble size is maintained at its minimum, very close to the average pore size. As a result, the fraction of trapped gas saturation ( $X_t$ ) is uniform and kept at its maximum (Fig. 4.10(a)). Second, even though the velocity decreases away from the well, water saturation

decreases (Fig. 4.9(a)) and the sweep efficiency is improved away from the well. The observation is consistent with the plots of foam mobility (Fig. 4.9(c)) and MRF (Fig. 4.9(d)) which make foam less mobile as a function of distance. (This may seem counter-intuitive because higher velocity is believed to make foams more viscous leading to lower water saturation; the result indeed is reasonable because strong foam in the low-quality regime is highly shear thinning, however.) Third and last, pressure decreases with radial distance, as expected, but the decrement is less than that of constant-MRF case in radial geometry, because of more viscous foams away from the well (Fig. 4.9(b)).

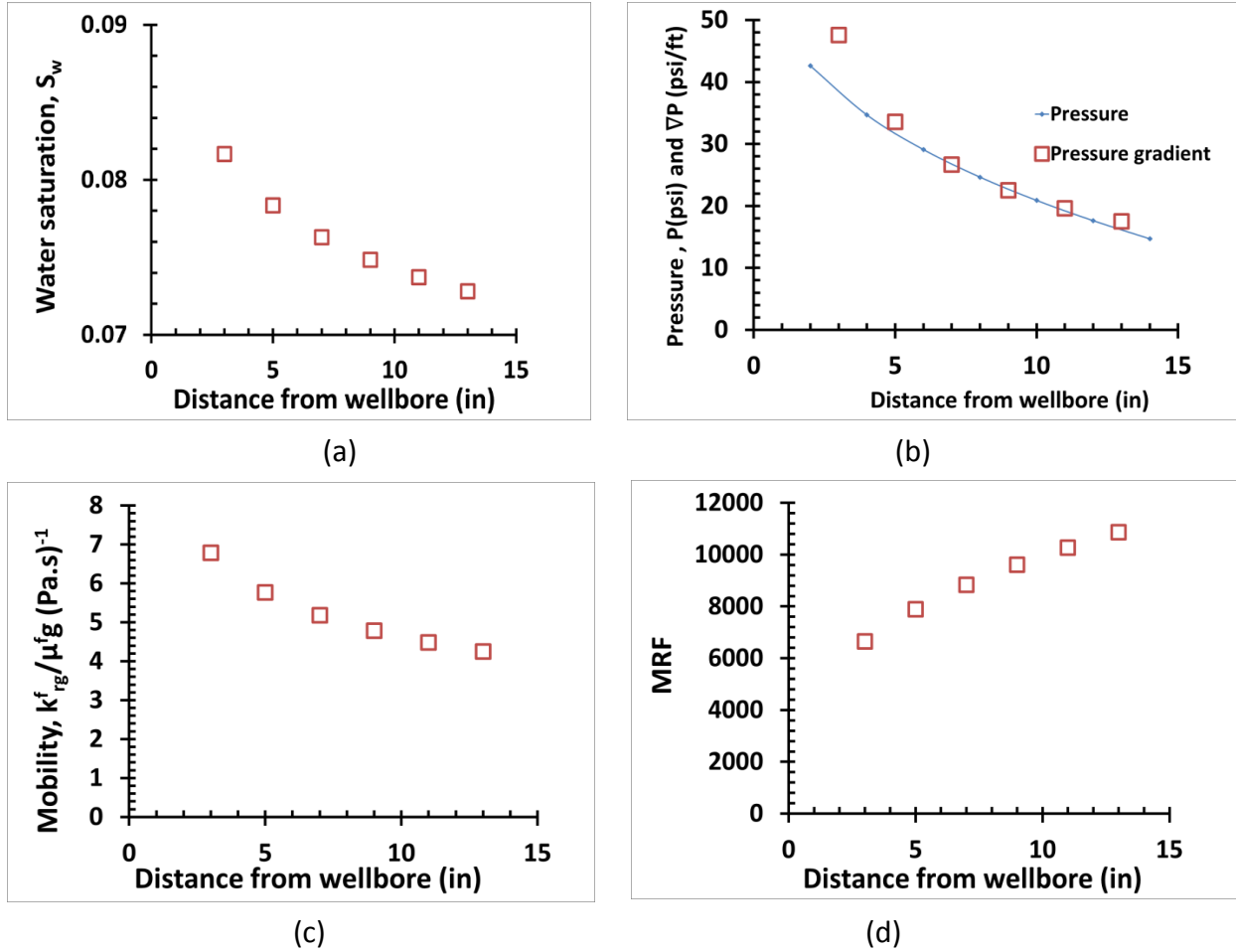


Fig. 4.9 Base-case calculation results showing the steady state after foam flooding (strong foams in the low-quality regime injected): (a) water saturation ( $S_w$ ); (b) pressure ( $P$  and  $\nabla P$ ); (c) mobility ( $k_{rg}^f / \mu_g^f$ ); and (d) mobility reduction factor (MRF)

The base-case example is extended to the case of strong foam in the high-quality regime, which requires the injection foam quality ( $f_g$ ) greater than  $f_g^*$ . Figs. 4.11 and 4.12 show the results of high-quality strong-foam case when  $f_g$  is set to be 0.99 (instead of  $f_g = 0.80$  in the base case) keeping all other parameters the same (note that  $f_g = 0.99$  falls in the high-quality regime as shown in Fig. 4.1).

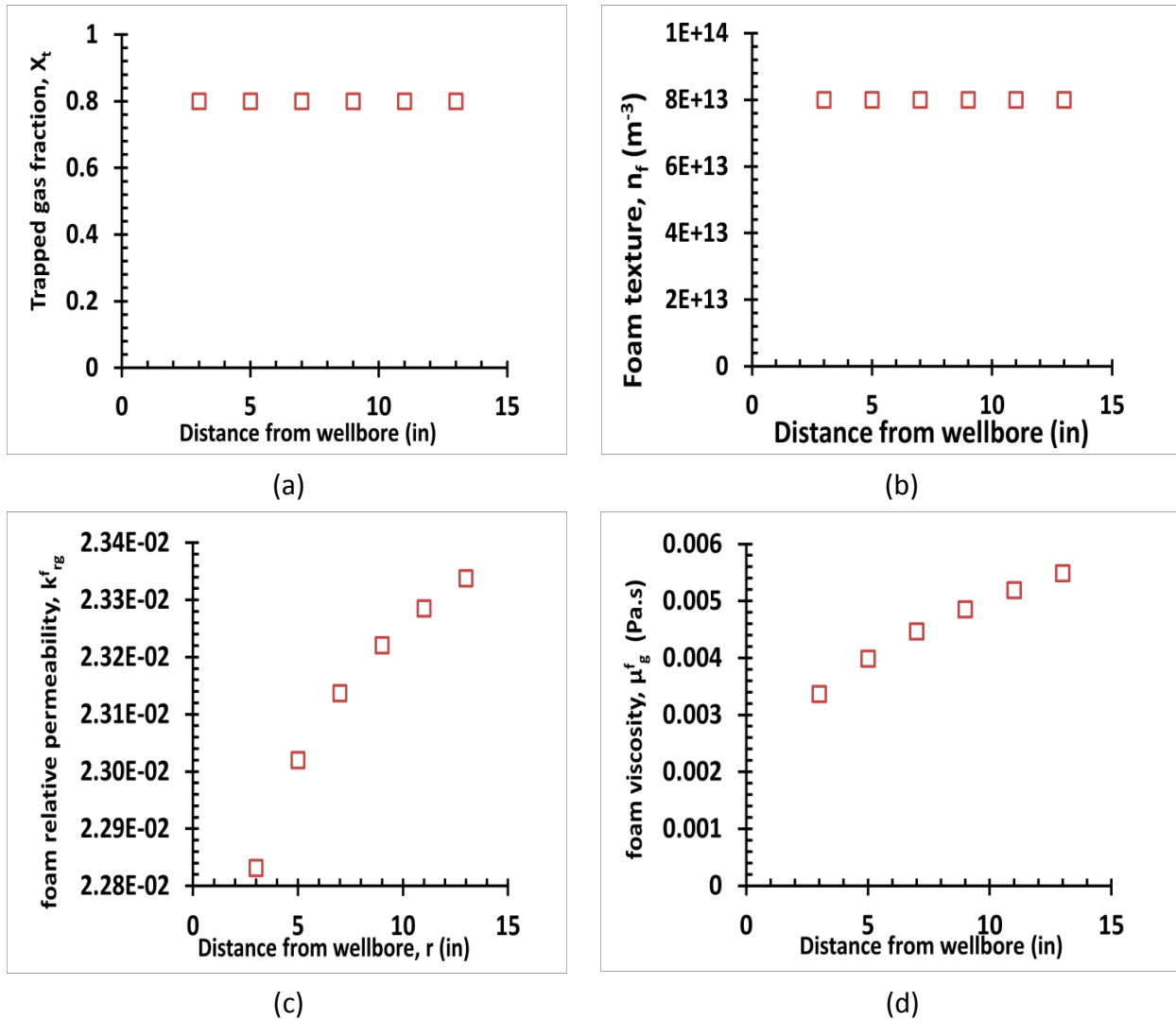
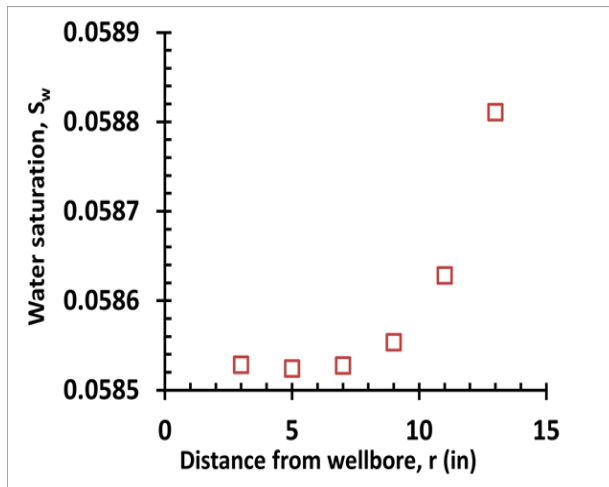
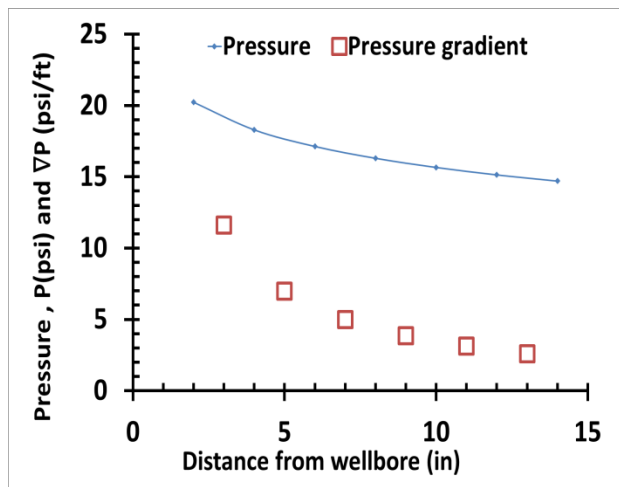


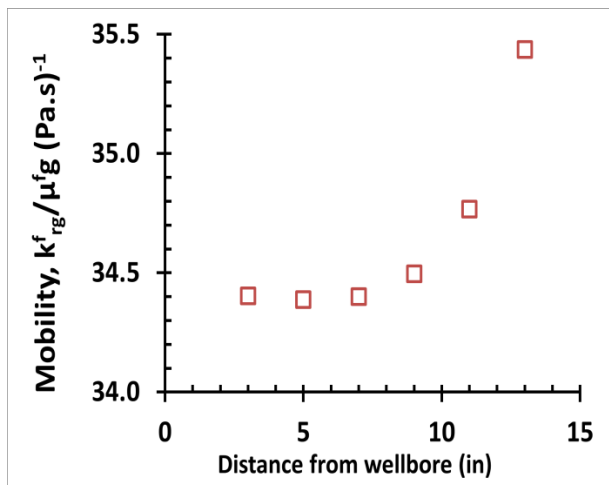
Fig. 4.10 Base-case calculation results showing the steady state after foam flooding (strong foams in the low-quality regime injected): (a) trapped gas fraction ( $X_t$ ); (b) foam texture ( $n_f$ ); (c) foam relative permeability ( $k_{rg}^f$ ); and (d) foam viscosity ( $\mu_g^f$ )



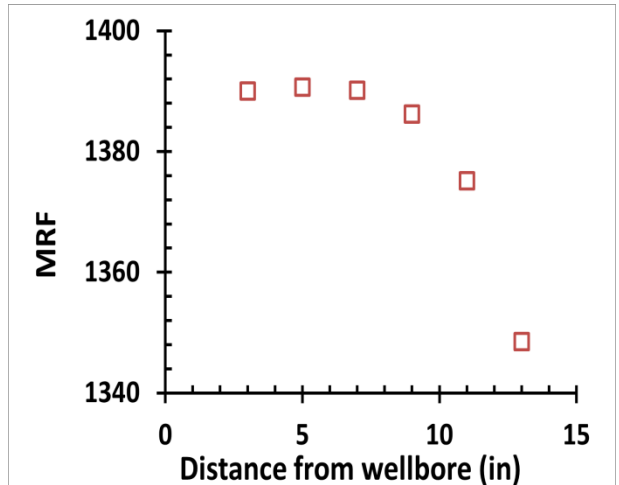
(a)



(b)



(c)



(d)

Fig. 4.11 Extension of base case calculation results showing the steady state after foam flooding (strong foams in the high-quality regime injected): (a) water saturation ( $S_w$ ); (b) pressure ( $P$  and  $\nabla P$ ); (c) mobility ( $k_{rg}^f / \mu_g^f$ ); and (d) mobility reduction factor (MRF)



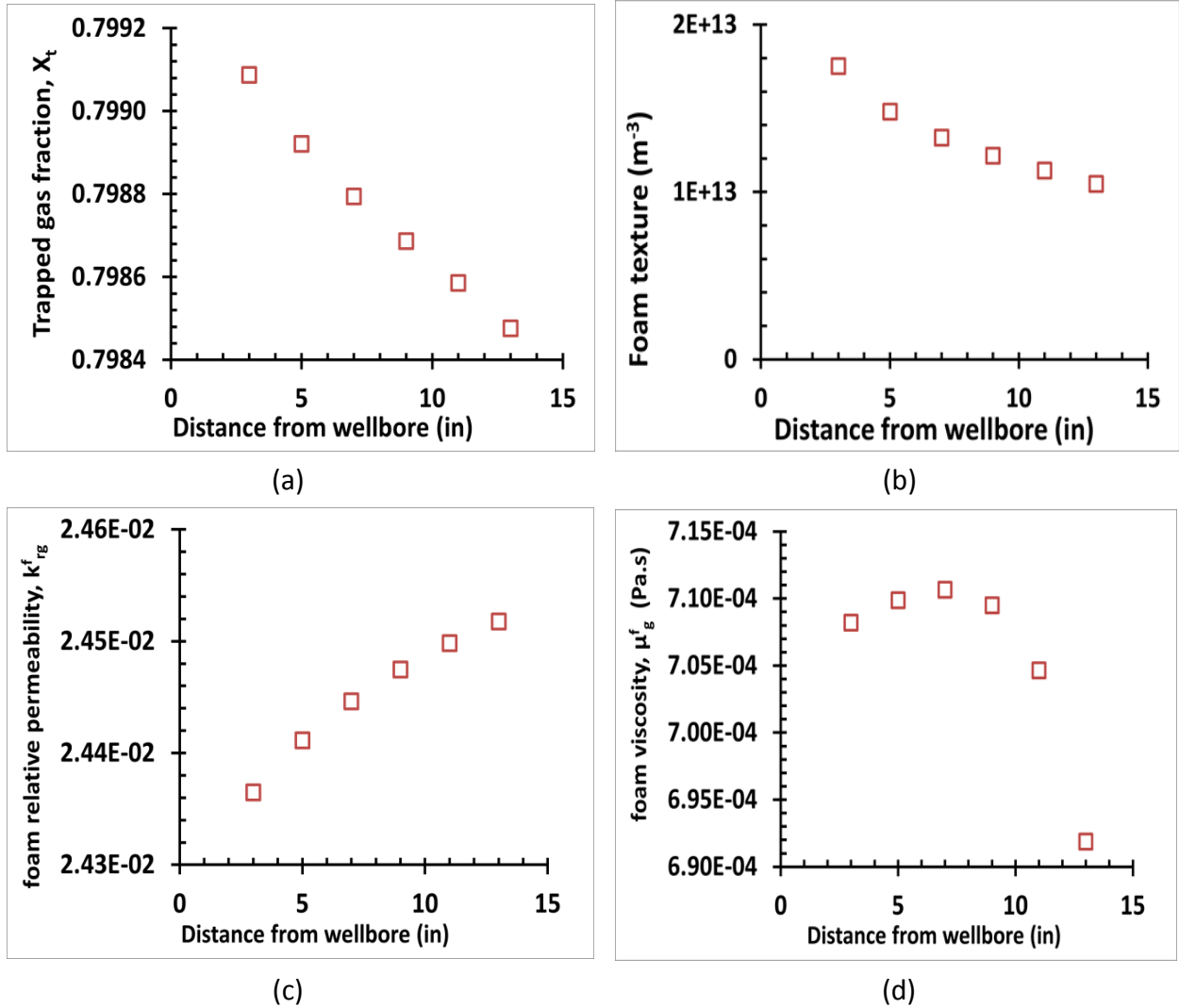


Fig. 4.12 Extension of base case calculation results showing the steady state after foam flooding (strong foams in the high-quality regime injected) (a) trapped gas fraction ( $X_t$ ); (b) foam texture ( $n_f$ ); (c) foam relative permeability ( $k_{rg}^f$ ); and (d) foam viscosity ( $\mu_g^f$ )

A few interesting observations can also be made for the propagation of strong foams in the high-quality regime. First, foam texture is significantly lower than  $n_{fmax}$  and declines with radial distance (Fig. 4.12(b)), meaning that foam becomes coarser away from the well and, as a result, the fraction of trapped gas saturation ( $X_t$ ) also declines with distance (Fig. 4.12(a)). Second, foam viscosity increases with distance near the well, but decreases away from the well. This behavior is a combined outcome of foam texture and velocity primarily (Eq. 3.15). As a result, such a behavior can also be found in other plots such as foam mobility, MRF, and water saturation (for example, MRF slightly goes up near the well but goes down away from the well with distance). Third and last, pressure decreases with radial distance, as expected, but the decrement is less rapid near the well (because of increasing MRF) and more rapid away from the well (because of decreasing MRF) than that of constant-MRF case in radial geometry (Fig. 4.11(b)).

The base-case example is extended to the case of weak foam by using  $q_t = 6.58 \times 10^{-7} \text{ m}^3/\text{s}$  (rather than  $q_t = 1.33 \times 10^{-5} \text{ m}^3/\text{s}$  of the base case) and injection foam quality of  $f_g = 0.80$ . This  $q_t$  value provides  $u_t$  values of  $1.35 \times 10^{-5}$ ,  $8.12 \times 10^{-6}$ ,  $5.80 \times 10^{-6}$ ,  $4.51 \times 10^{-6}$ ,  $3.69 \times 10^{-6}$ , and  $3.12 \times 10^{-6} \text{ m/s}$  for  $u_{t1}$  through  $u_{t6}$  for the 6 grid block system (Fig. 4.4). Note that these six points are positioned in the bottom part of the S-shaped curve (cf. Fig. 4.6).

Figs. 4.13 and 4.14 show the results of weak-foam case, keeping all other parameters the same as the base case except for  $q_t$  and  $f_g$ . The response of weak-foam propagation can be summarized as follows: foam texture becomes coarser away from the well, and thus water saturation and foam mobility increase but MRF and trapped gas saturation decrease with radial distance.

It should be noted that in all calculations, the grid block size ( $\Delta r$ ) of 2 inches is used. Additional calculations are performed by using the grid block size ( $\Delta r$ ) of 0.5 and 1.0 inches and, as shown in Fig. 4.15, the results are shown to be almost the same for the base case with  $\Delta r = 2$  inches. This confirms that the use of  $\Delta r = 2$  inches in this study is reasonable.

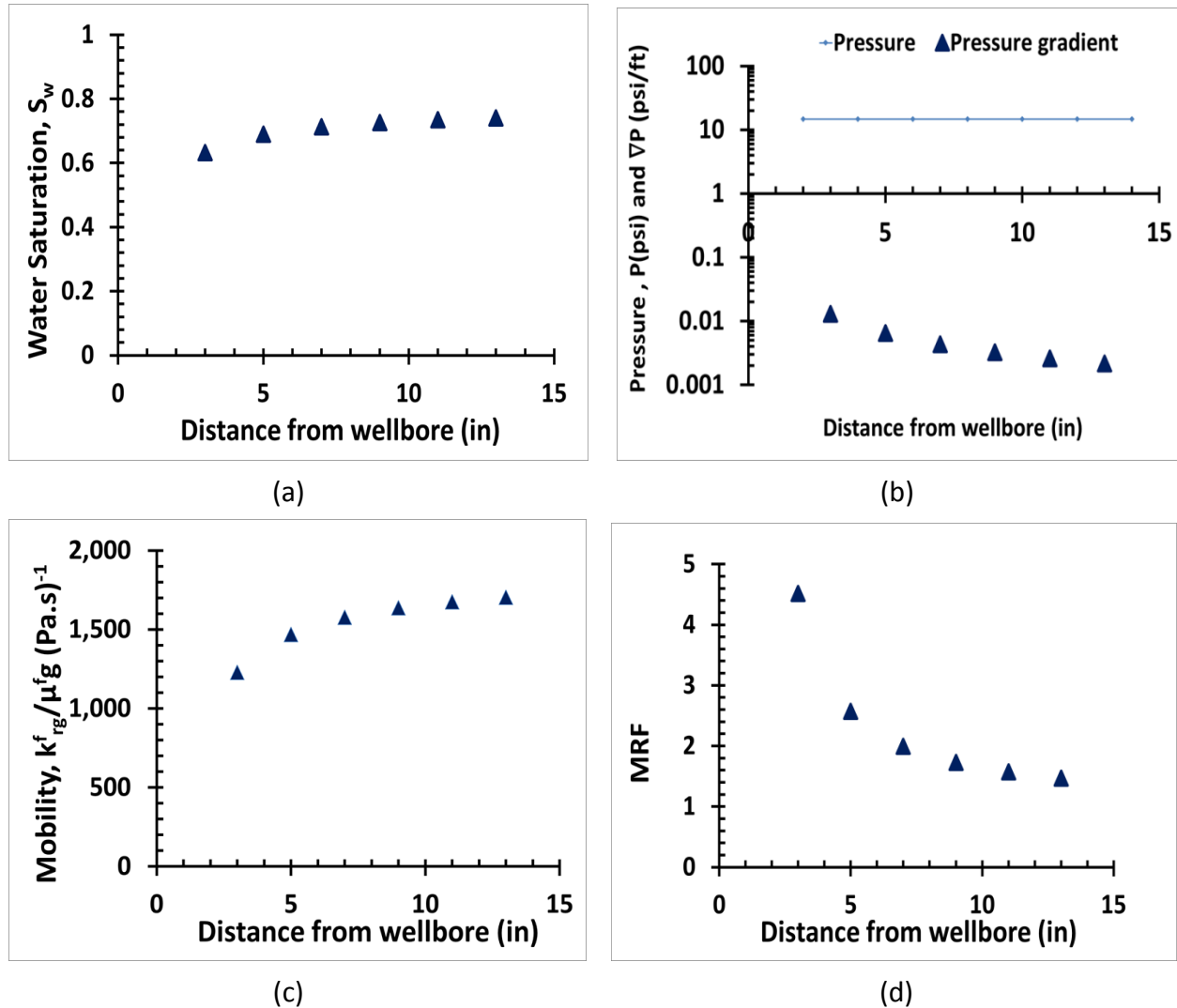
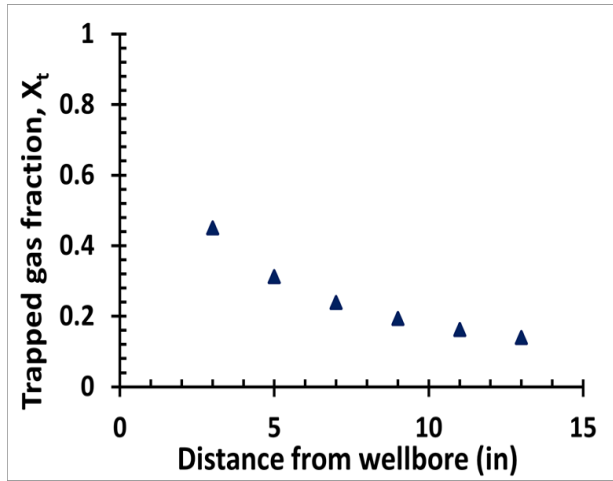
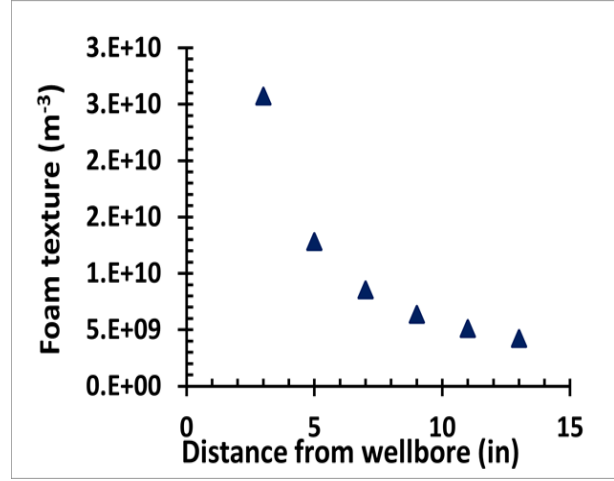


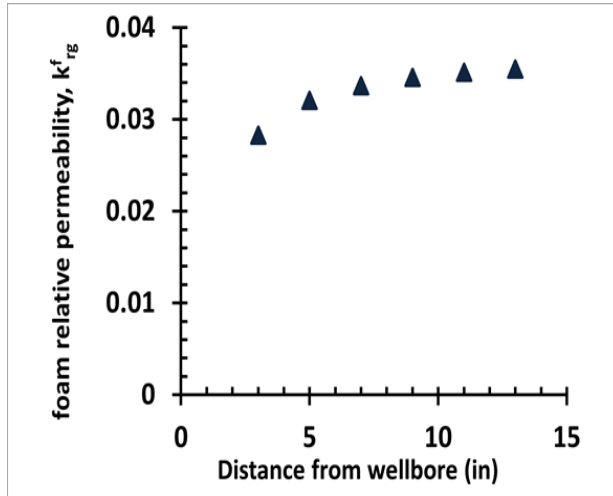
Fig. 4.13 Extension of base case calculation results showing the steady state after foam flooding (weak foams injected): (a) water saturation ( $S_w$ ); (b) pressure ( $P$  and  $\nabla P$ ); (c) mobility ( $k_{rg}^f / \mu_g^f$ ); and (d) mobility reduction factor (MRF)



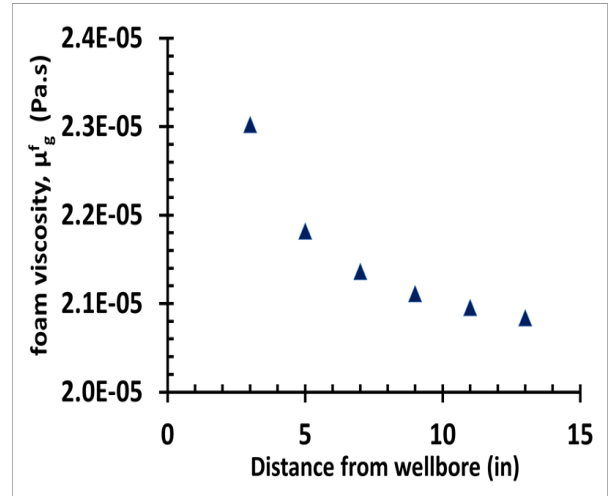
(a)



(b)



(c)



(d)

Fig. 4.14 Extension of base case calculation results showing the steady state after foam flooding (weak foams injected): (a) trapped gas fraction ( $X_t$ ); (b) foam texture ( $n_f$ ); (c) foam relative permeability ( $k^f_{rg}$ ); and (d) foam viscosity ( $\mu^f_g$ )

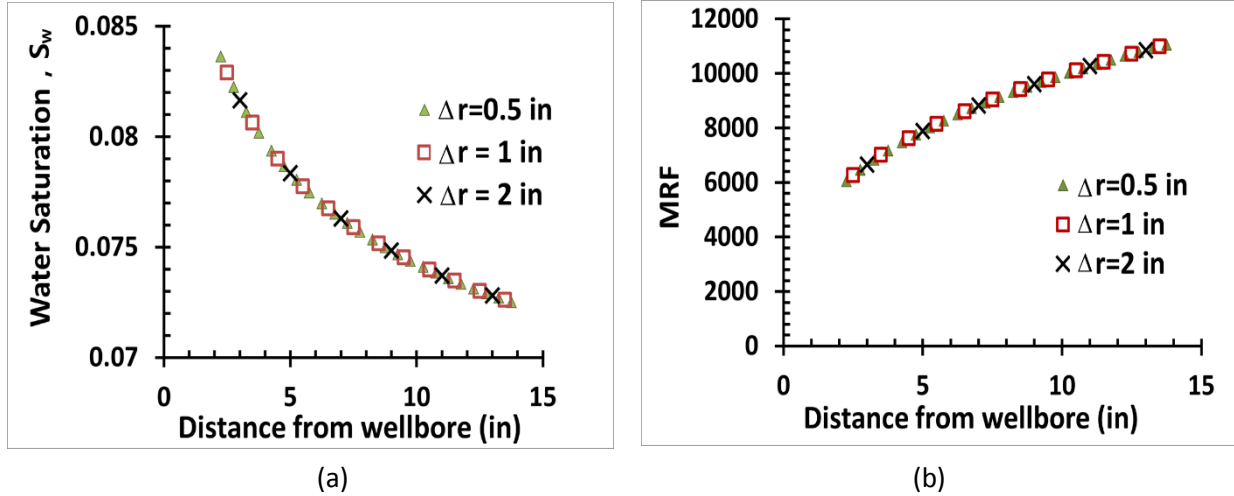


Fig. 4.15 Calculation results comparing three grid block sizes ( $\Delta r = 0.5, 1$ , and  $2$  inches): (a) water saturation and (b) mobility reduction factor ( $\Delta r = 2$  inch is selected in this study)

#### 4.2. Effect of input parameters

Injection foam quality is an important parameter to decide in foam applications. In addition to those two foam qualities investigated earlier for strong foam propagation ( $f_g = 0.80$  and  $f_g = 0.99$ ), other injection foam quality values are also considered such as  $f_g = 0.98$  and  $0.65$  at  $q_t = 1.33 \times 10^{-5} \text{ m}^3/\text{s}$ . Note that  $f_g^*$  is about  $0.80 - 0.92$  in this case (see Fig. 4.3).

Fig. 4.16 shows the results in terms of water saturation ( $S_w$ ), pressure ( $P$  and  $\nabla P$ ), mobility reduction factor (MRF), and foam texture ( $n_f$ ). One can find a few interesting aspects. First, water saturation for strong foams in the high-quality regime ( $f_g = 0.98$  and  $f_g = 0.99$ ) stays almost the same near the limiting water saturation ( $S_w^* = 0.0585$ ) as expected. On the other hand, water saturation for strong foams in the low-quality regime ( $f_g = 0.65$  and  $f_g = 0.80$ ) decreases with distance (as expected from the base case) showing higher water saturation at wetter injection condition. Second, foam texture stays at the maximum foam texture for foams in the low-quality regime, but becomes lower at drier injection conditions. Third and last, pressure and mobility

reduction factor change more for foams in the high-quality regime because foam texture varies significantly to get adjusted to the injection condition. Note that the pattern observed in the base case still exists – mobility reduction factor increases with distance for foams in the low-quality regime, but decreases for foams in the high-quality regime.

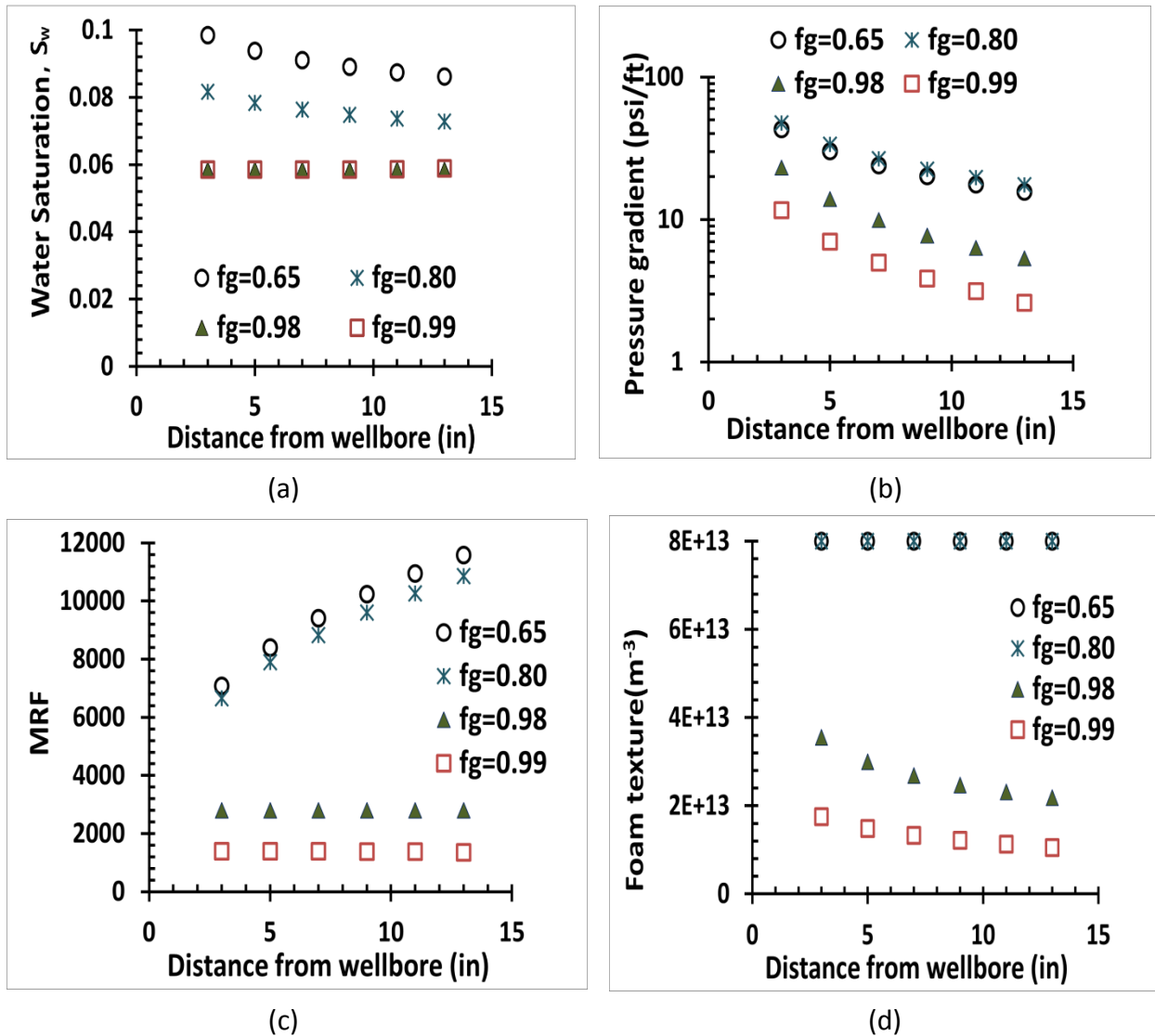


Fig. 4.16 Calculation results showing the steady state after foam flooding (strong foams injected) at various foam qualities: (a) water saturation ( $S_w$ ); (b) pressure gradient ( $\nabla P$ ); (3) MRF; and (4) foam texture ( $n_f$ )

Another important parameter to be decided in the field is total injection rate ( $q_t$ ), because it should be high enough to create and migrate fine-textured foams deep into the reservoir but should be low enough not to fracture the wellbore region. In addition to the base case where  $q_t = 1.33 \times 10^{-5} \text{ m}^3/\text{s}$  and  $f_g = 0.80$ , two other  $q_t$  values of  $1.33 \times 10^{-4} \text{ m}^3/\text{s}$  and  $1.33 \times 10^{-3} \text{ m}^3/\text{s}$  are selected at the same  $f_g$  to check how the response changes as shown in Fig. 4.17. The results show that as long as strong foams in the same low-quality regime are obtained, the general trend seems pretty consistent. As expected, higher rate induces higher pressure gradient and lower MRF. Fig. 4.18 shows similar calculations for foams in the high-quality regime, comparing the cases of  $q_t = 1.33 \times 10^{-5}$ ,  $1.33 \times 10^{-4}$ , and  $1.33 \times 10^{-3} \text{ m}^3/\text{s}$  all at the same  $f_g$  of 0.99. The results show that similar to strong foam in the low-quality regime, higher rate induces higher pressure gradient but does not affect  $S_w$  and MRF significantly.

During earlier foam injection in a thick reservoir, the flow pattern can be spherical rather than radial. The difference between these two cases within the context of this modeling study is that the velocity declines more rapidly with distance in a spherical system compared to a radial system. This implies that the foam characteristic observed in a radial geometry compared to a linear geometry becomes more pronounced. Figs. 4.19 and 4.20 show the results comparing both cases at  $q_t = 1.33 \times 10^{-5} \text{ m}^3/\text{s}$  for  $f_g = 0.80$  and  $f_g = 0.95$ , respectively. As expected the trends in both radial and spherical cases are similar, but the magnitude of the change is more significant in a spherical geometry (The last data point representing the 6<sup>th</sup> grid block is off the trend because it falls into the weak-foam state, and therefore is ignored in this analysis). For  $f_g = 0.80$ , the pressure drops in linear and spherical geometries are 62.8 psi and 14.1 psi from mechanistic calculations, respectively, over the distance of 12 inches at  $q_t = 1.33 \times 10^{-5} \text{ m}^3/\text{s}$ , which gives the

ratio of 4.5 (i.e., 62.8/14.1). For  $f_g = 0.95$ , the ratio is 5.3 because the pressure drops are 67.0 psi and 12.7 psi in linear and spherical geometries. These ratio values are similar to that measured by Li et al. (2006), which was 5, in their one- and three-dimensional foam displacement experiments with gas injection into surfactant filled sand pack and tank.

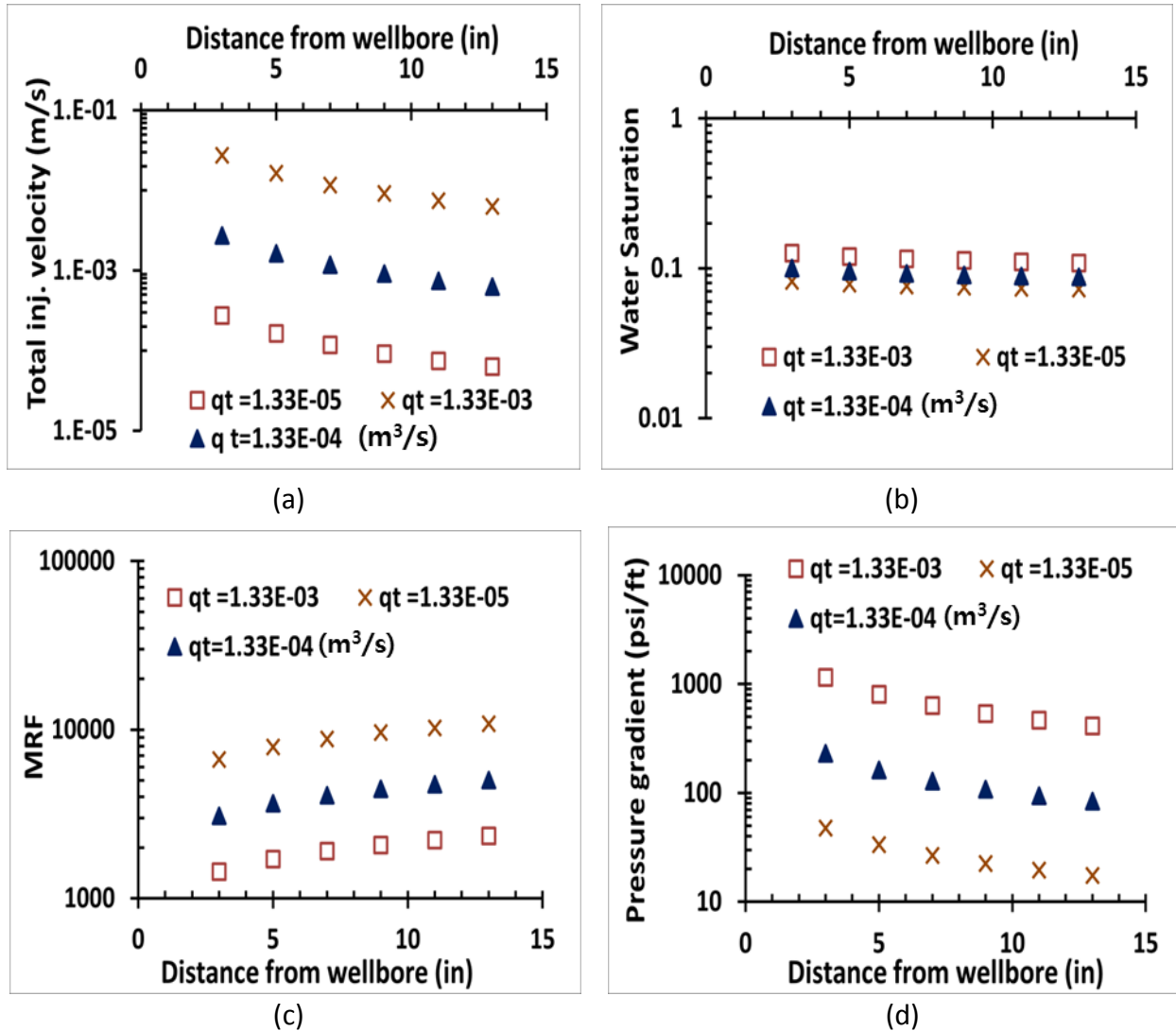
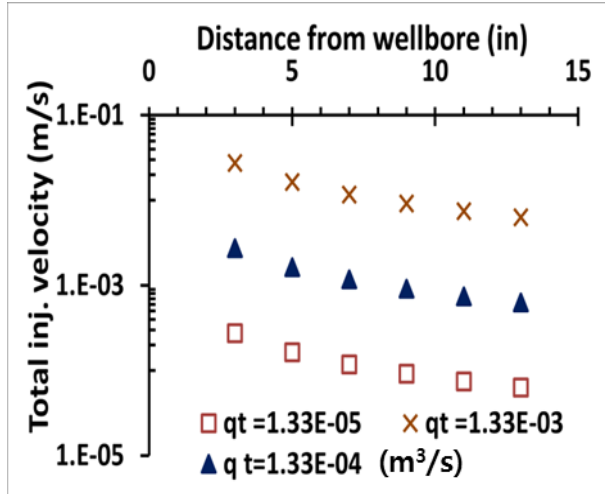
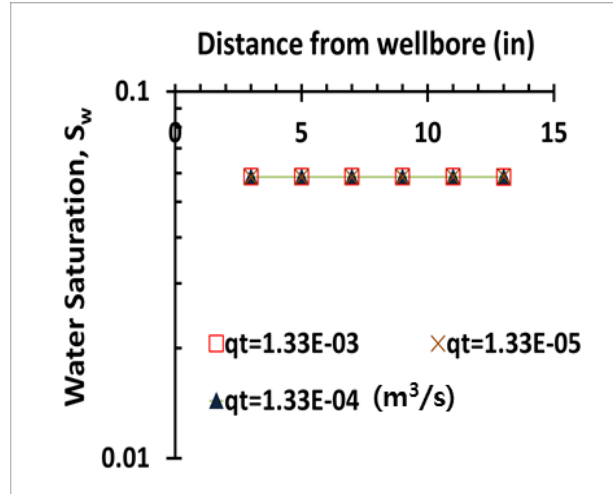


Fig. 4.17 Calculation results showing the steady state after foam flooding (strong foams in the low-quality regime injected;  $f_g = 0.80$ ) at various injection rates: (a) total injection velocity ( $u_t$ ); (b) water saturation ( $S_w$ ); (c) pressure gradient ( $\nabla P$ ); and (d) MRF

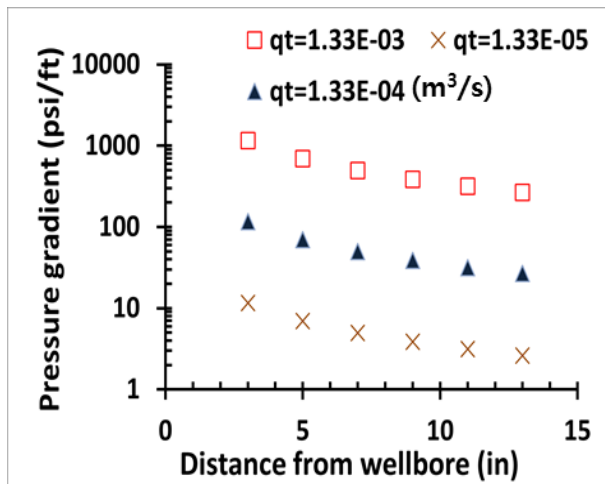




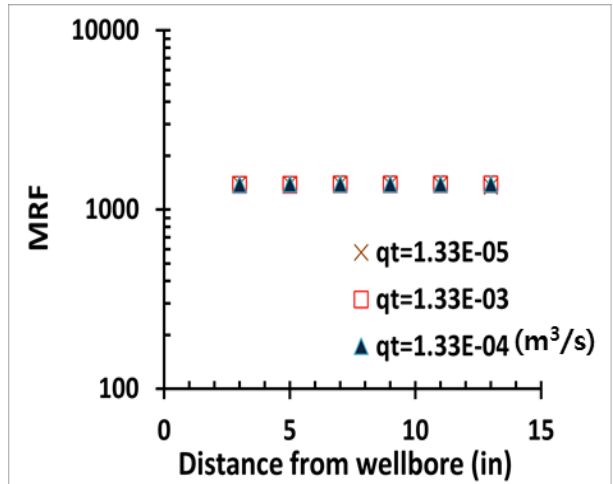
(a)



(b)

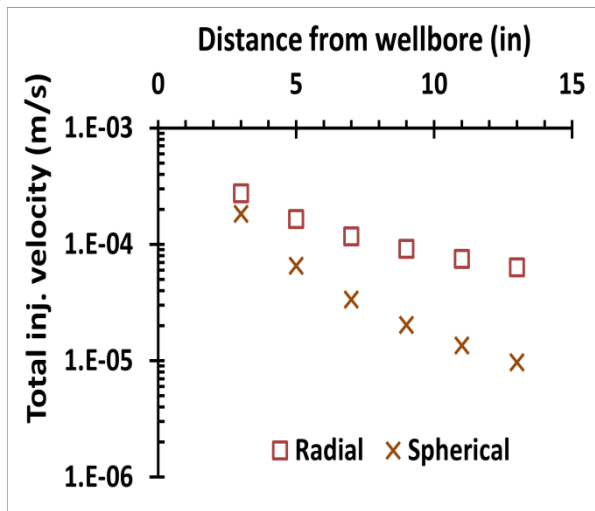


(c)

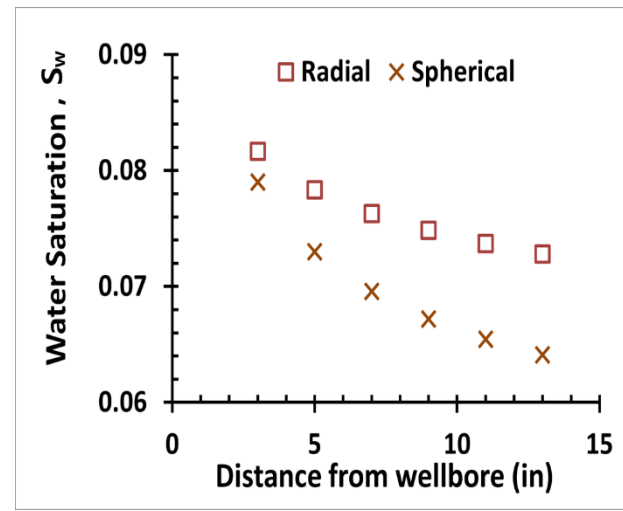


(d)

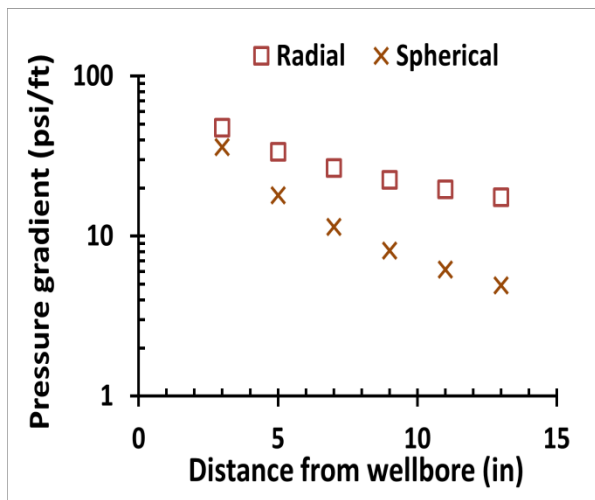
Fig. 4.18 Calculation results showing the steady state after foam flooding (strong foams in the high-quality regime injected;  $f_g = 0.99$ ) at various injection rates: (a) total injection velocity ( $u_t$ ); (b) water saturation ( $S_w$ ); (c) pressure gradient ( $\nabla P$ ); and (d) MRF



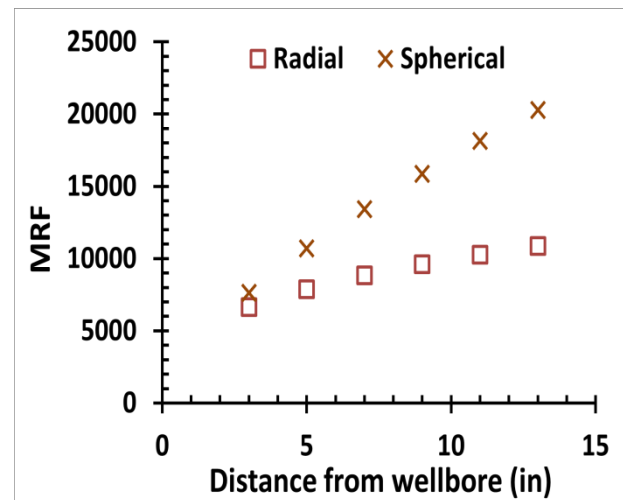
(a)



(b)

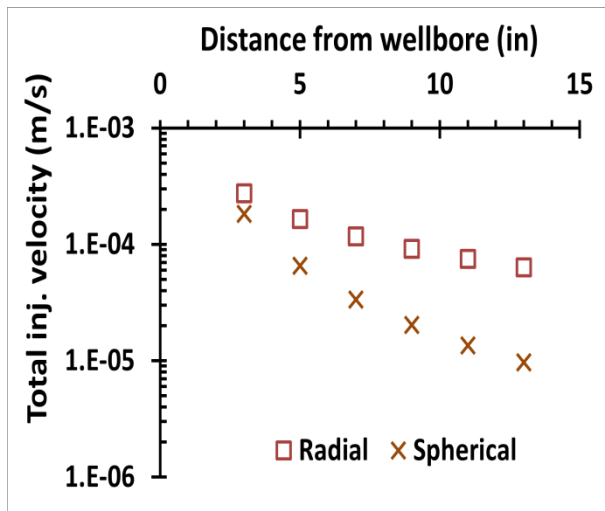


(c)

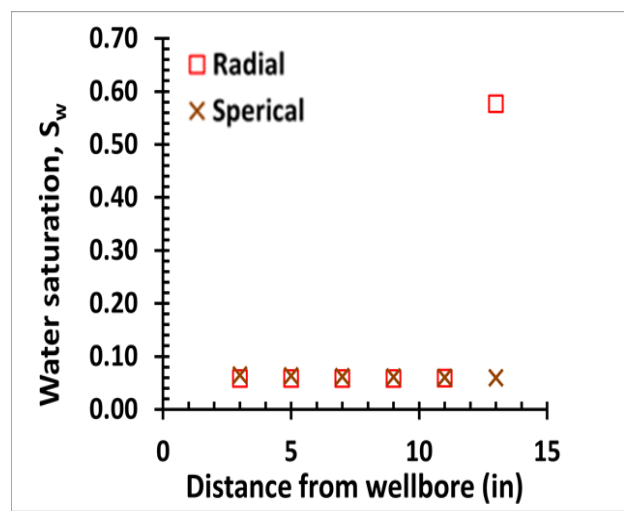


(d)

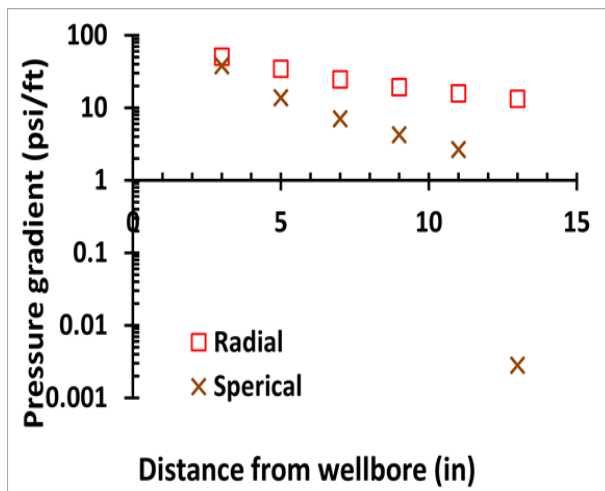
Fig. 4.19 Calculation results showing the steady state after foam flooding (strong foams injected;  $q_t = 1.33 \times 10^{-5} \text{ m}^3/\text{s}$  and  $f_g = 0.80$ ) at different systems: (a) total injection velocity ( $u_t$ ); (b) water saturation ( $S_w$ ); (c) pressure gradient ( $\nabla P$ ); and (d) MRF



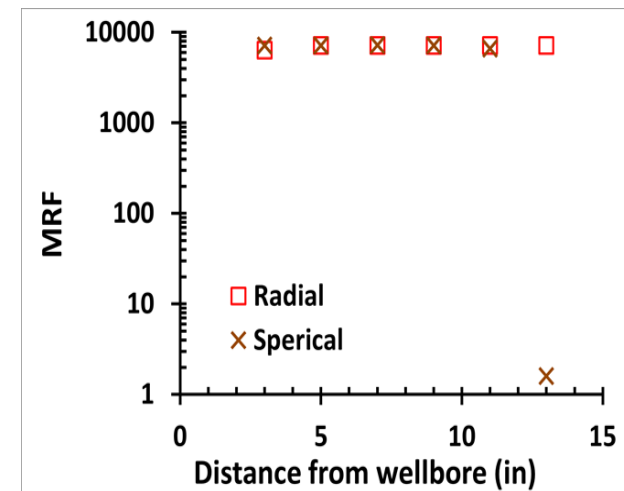
(a)



(b)



(c)



(d)

Fig. 4.20 Calculation results showing the steady state after foam flooding (strong foams injected;  $q_t = 1.33 \times 10^{-5} \text{ m}^3/\text{s}$  and  $f_g = 0.95$ ) at different systems: (a) total injection velocity ( $u_t$ , m/s); (b) water saturation ( $S_w$ ); (c) pressure gradient ( $\nabla P$ ); and (d) MRF

### 4.3. Implications in field-scale foam processes

The example base-case calculations assuming a strong-foam state throughout the system may not be necessarily true in field treatments, because strong foam injected at the wellbore essentially turns into weak-foam state as it propagates. Therefore, it is crucial to estimate how far injected strong foam can propagate in foam EOR processes. A literature review is first conducted, as summarized in Table 4.3, showing the range of injection rate and injection foam quality in field applications. This study chooses model input parameters similar to the conditions given by Rangely Weber Sand Unit (Jonas et al., 1990) which has wellbore radius ( $r_w$ ) of 5 in, external radius ( $r_e$ ) of 330 ft, total injection rate ( $q_t$ ) of  $5.89 \times 10^{-3} \text{ m}^3/\text{s}$ , injection foam quality ( $f_g$ ) of 0.77. For modeling purpose, the reservoir is assumed to have a perfectly radial geometry with the uniform thickness of 27.5 ft. (This is 10 times thinner than the average reservoir thickness of 275 ft in order to consider only radial flow). Each grid block size is chosen to be 2 ft.

Table 4.3 Foam field tests with injection condition

Field	Year	Injection method	Injection rate (m <sup>3</sup> /s)	Foam quality
Midway sunset, CA	1989-90	Steam with surfactant & N <sub>2</sub>	$5.82 \times 10^{-3}$	N.A.*
Kern river, CA	1980-85, 1982-86	Steam with surfactant & N <sub>2</sub>	$4.59 \times 10^{-4}$	N.A.*
North ward-estate, TX	1990- 91	Surfactant-CO <sub>2</sub> Alternate	$1.56 \times 10^{-3}$	0.5-0.8
Siggins, IL	1964- 66	Foam-air	$1.54 \times 10^{-2}$	0.9
Rangely Weber Sand Unit, CO	1989	CO <sub>2</sub> -foam co-injection	$5.89 \times 10^{-3}$	0.77
East Vacuum Grayburg/San Andres Unit, NM	1993	CO <sub>2</sub> -foam injection	$1.84 \times 10^{-3}$	0.75

(\*: foam quality was not provided, but steam quality was 0.5 in both cases.)

The transition from strong-foam state to weak-foam state in field-scale applications is conceptually shown in Fig. 4.21. Suppose an S-shaped curve ( $\nabla P$  vs.  $u_t$  at given  $f_g$ ) showing three foam states is determined by laboratory experiments (Fig. 4.21(a)). As foams injected at the wellbore propagate into the reservoir, the velocity and pressure gradient decrease gradually (following ①). When the velocity reaches the threshold velocity ( $u_{sf}$ ), the condition abruptly shifts from strong-foam to weak-foam state (②) and further beyond foam propagates deeper into the reservoir in a weak-foam state (③). The same concept is shown in Fig. 4.21(b) where the presence of threshold velocity ( $u_{sf}$ ) is translated into the threshold radial distance ( $r_{sf}$ ). This  $r_{sf}$  value can be determined by

$$r_{sf} = \frac{q_t}{2\pi u_{sf} h} \quad (4.1)$$

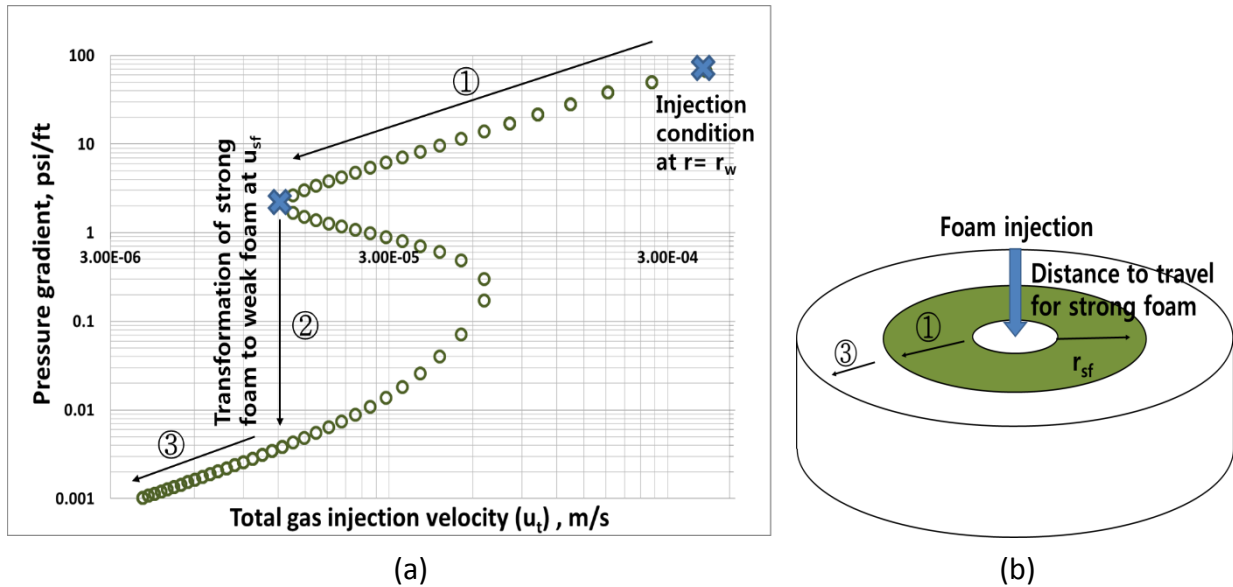


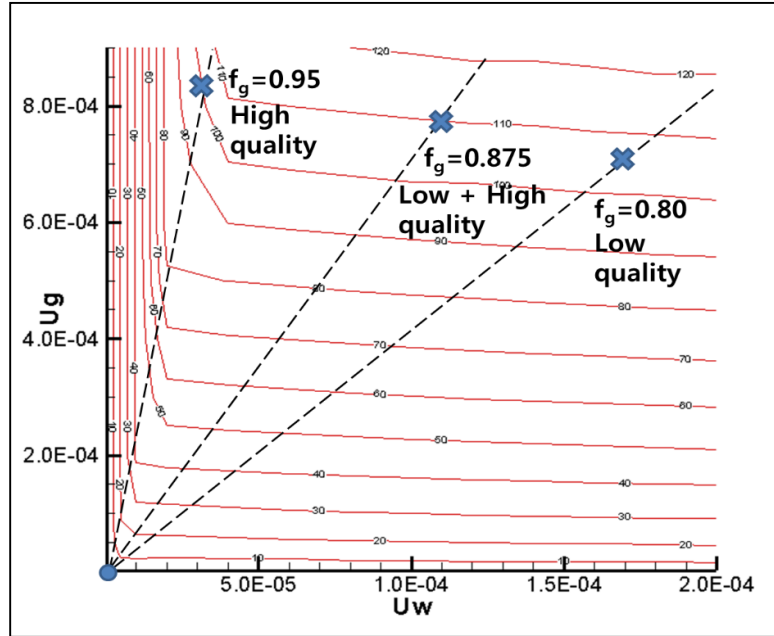
Fig. 4.21 A schematic showing the transition from strong-foam to weak-foam state at the threshold velocity of  $u_{sf}$  and threshold distance of  $r_{sf}$

For  $f_g = 0.99, 0.98, 0.95, 0.875, 0.80, 0.725, 0.60,$  and  $0.525$  at  $q_t = 5.89 \times 10^{-3} \text{ m}^3/\text{s}$  (base case), the  $u_{sf}$  values are  $5.00 \times 10^{-5}, 2.50 \times 10^{-5}, 1.36 \times 10^{-5}, 5.79 \times 10^{-6}, 3.20 \times 10^{-6}, 3.00 \times 10^{-5}, 3.00 \times 10^{-5},$  and  $3.00 \times 10^{-5} \text{ m/s}$  respectively, which correspond to the  $r_{sf}$  values of 7.5, 15.4, 27.0, 60.0, 93.4, 95.4, 103.4, and 105.4 ft. This result implies that  $r_{sf}$  for strong foam with low  $f_g$  does not vary significantly (95.4 to 105.4) but  $r_{sf}$  for strong foam with high  $f_g$  does (7.5 to 60.0).

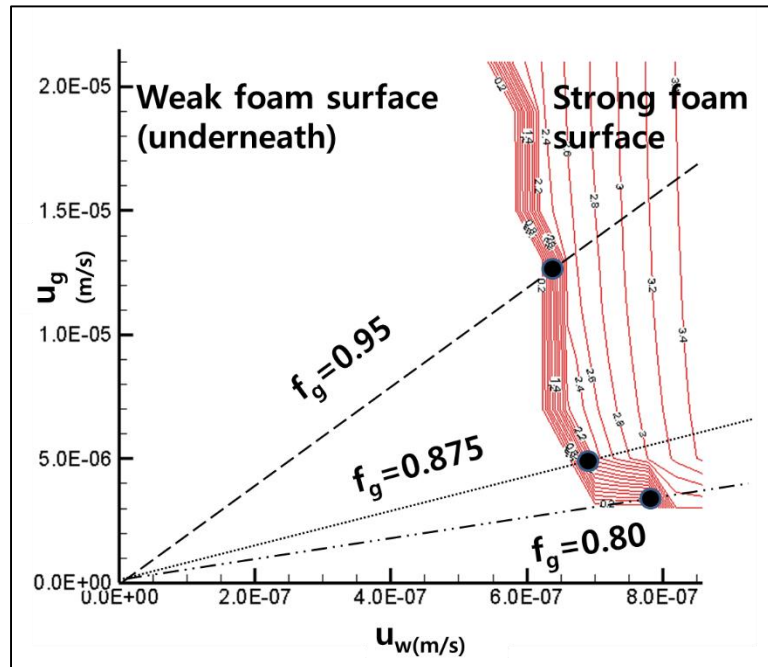
In order to check foam characteristics over the reservoir scale, three foam qualities are considered at the same  $q_t$  of  $5.89 \times 10^{-3} \text{ m}^3/\text{s}$ :  $f_g = 0.80, 0.875,$  and  $0.95$ . Fig. 4.22 shows the paths for each of those three injection conditions. Note that X symbols represent the conditions at the wellbore and O symbols represent the points where strong foams turn into weak foams. It should be pointed out that  $f_g = 0.80$  is the case where there is only strong foams in the low-quality regime before turning into weak foams. Similarly,  $f_g = 0.95$  is the case where there is only strong foams in the high-quality regime, while  $f_g = 0.875$  is the case where strong foams are initially in the low-quality regime but moves into the high-quality regime before turning into weak foams.

Figs. 4.23 through 4.25 compare the results of these three cases. A few interesting aspects are observed. First, the distance to travel before turning into weak foam ( $r_{sf}$ ) is about 93, 60, and 27 ft for  $f_g = 0.80, 0.875,$  and  $0.95,$  respectively, implying that strong foams in the low-quality regime can travel farther compared to other cases. Second, MRF of strong foams increases with radial distance for  $f_g = 0.80,$  but stays almost the same (or slight increase followed by slight decrease) for  $f_g = 0.95$ . The case of for  $f_g = 0.875$  shows a combination of both. This is consistent with the results with the base case. Third, the change in MRF is much more significant for  $f_g = 0.80$  (MRF = 6781 at  $r_w$  to MRF = 27478 at  $r_{sf}$ ) compared to  $f_g = 0.95$  (MRF = 6456 at  $r_w$  to MRF = 7208 (maximum) at  $r = 13\text{ft}$ ). This implies that the current practice of using a constant MRF in

foam simulation can lead to significant errors, especially, for strong foams in the low-quality regime.



(a)



(b)

Fig. 4.22 Three different injection foam qualities to test foam characteristics in field-scale applications: (a) contour map showing injection conditions; and (b) contour map showing the positions corresponding to  $r_{sf}$

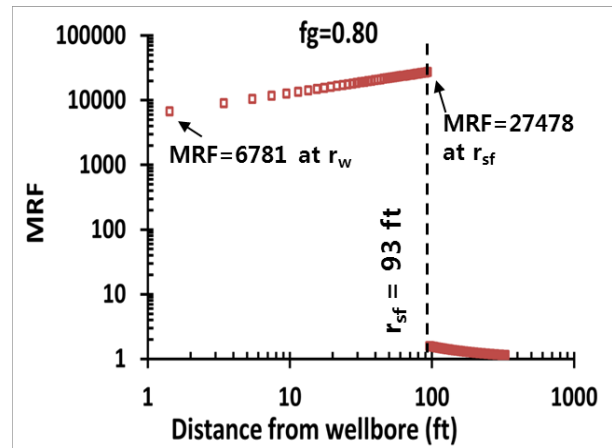
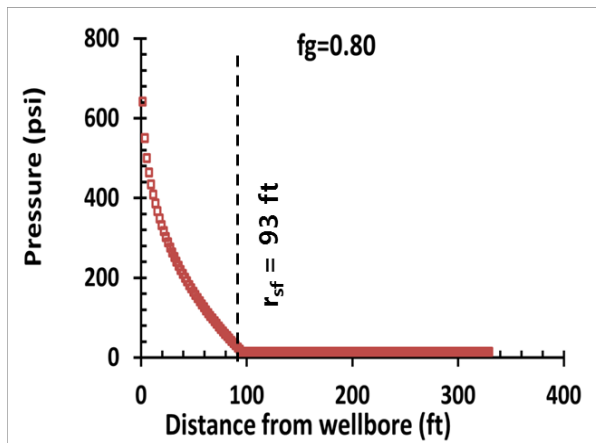


Fig. 4.23 Pressure and MRF profile along the reservoir at  $f_g = 0.80$

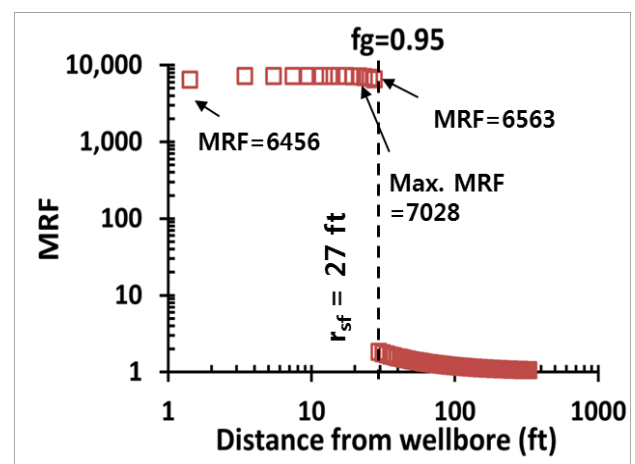
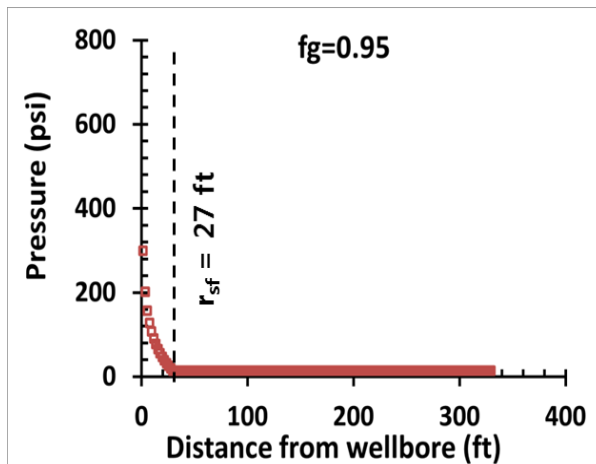


Fig. 4.24 Pressure and MRF profile along the reservoir at  $f_g = 0.95$

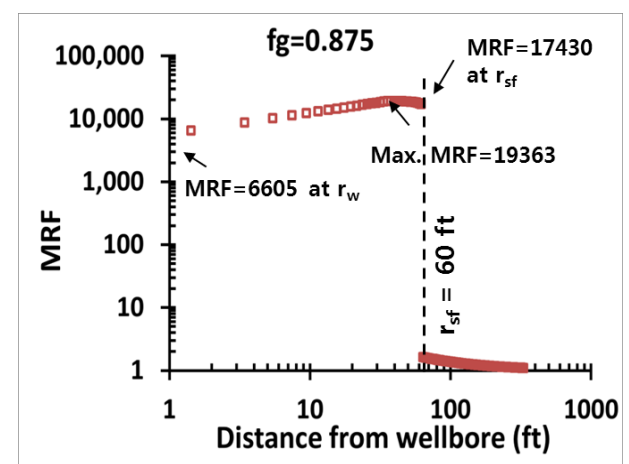
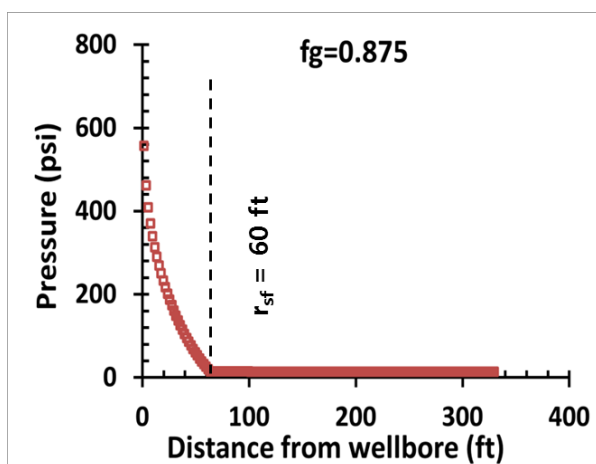


Fig. 4.25 Pressure and MRF profile along the reservoir at  $f_g = 0.875$



In order to check the effect of grid-block size in calculations, 10 times smaller grid block size (0.2 ft rather than 2 ft) is applied. The results in Figs. 4.26(a) through 4.26(c) showing pressure and MRF profiles along the reservoir at  $f_g = 0.80$ ,  $f_g = 0.95$ , and  $f_g = 0.875$  (cf, Fig. 4.23, 4.24, and 4.25 respectively). They reveal that inlet pressures for 0.2 ft grid-block size are 652, 573, and 311 psi, which compare with 643, 558, and 300 psi for 2 ft grid-block size, showing 1.4, 2.4, and 3.5% difference. The distances of strong foam propagation at the three  $f_g$  values for 2 ft and 0.2 ft are the same. Both conclude that the use of 2 ft grid block is reasonable for  $r_{sf}$  calculation.

Thinking of the fact that  $u_{sf}$  stays almost the same for strong foams in the low-quality regime and increases with  $f_g$  for strong foams in the high-quality regime (Fig. 4.3), the results in Fig. 4.23 through 4.25 imply that the distance to travel before turning into weak foam ( $r_{sf}$ ) is insensitive to  $f_g$  as long as the injection condition falls into the low-quality regime, while decreases sensitively to  $f_g$  once the injection condition is in the high-quality regime. Fig. 4.27 shows the plot illustrating how  $r_{sf}$  changes as a function of  $f_g$  at  $q_t = 5.89 \times 10^{-3} \text{ m}^3/\text{s}$  (Figs. 4.23-4.25),  $1.18 \times 10^{-2} \text{ m}^3/\text{s}$  (2 times higher), and  $2.95 \times 10^{-3} \text{ m}^3/\text{s}$  (2 time lower). Such a plot seems to be very helpful for the design of field foam applications.

How much difference would it make in terms of pressure profile if a constant value of MRF is applied compared to mechanistic modeling? Fig. 4.28 shows the comparison between the mechanistic model (this study) and a local-steady-state foam model using constant MRF. Two MRF values are selected at  $r = r_w$  and  $r = r_{sf}$  (taken from Figs. 4.23 and 4.24). The results show that the use of constant MRF value can lead to as much as -47 to 109 % error for foams in the low-quality regime, and as much as -10 to 12 % error for foams in the high-quality regime. This plot reveals why the use of varying MRF should be carefully considered in field-scale foam simulations.

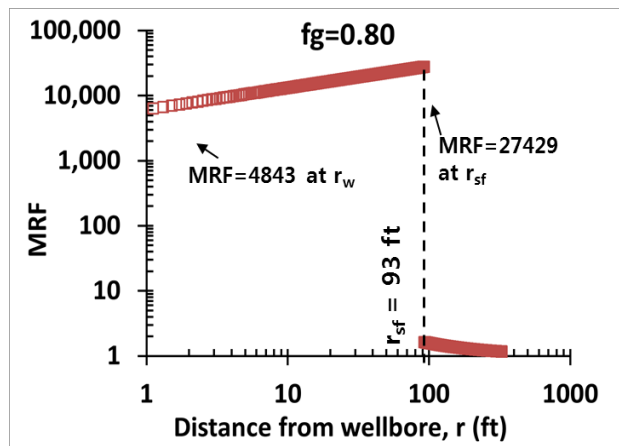
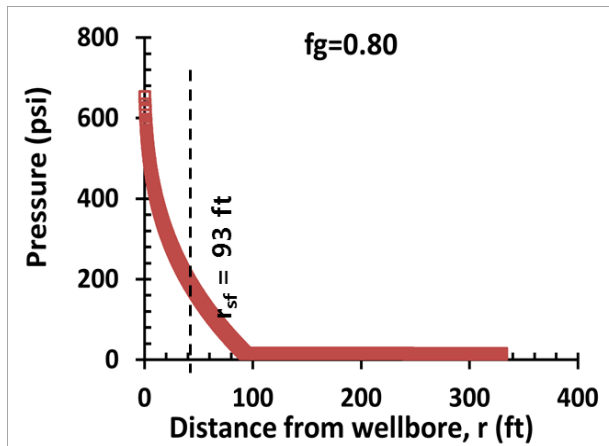


Fig. 4.26(a) Pressure and MRF profiles along the reservoir at  $f_g=0.80$  (grid block size 0.2 ft rather than 2 ft)

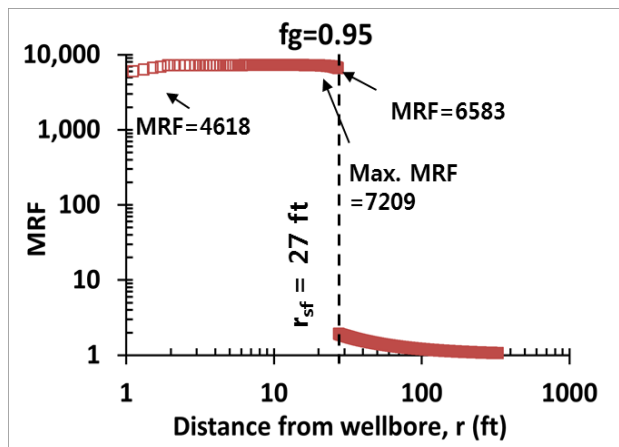
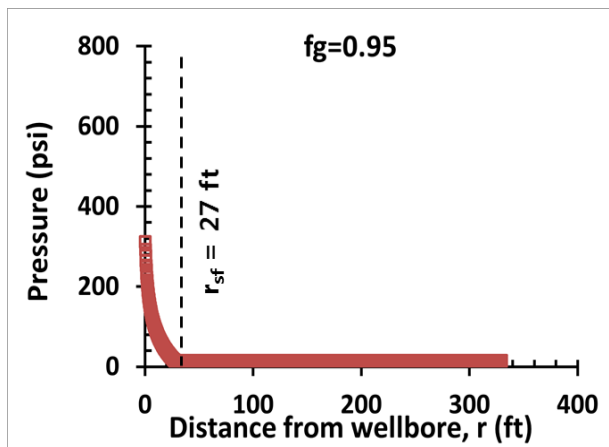


Fig. 4.26(b) Pressure and MRF profiles along the reservoir at  $f_g=0.95$  (grid block size 0.2 ft rather than 2 ft)

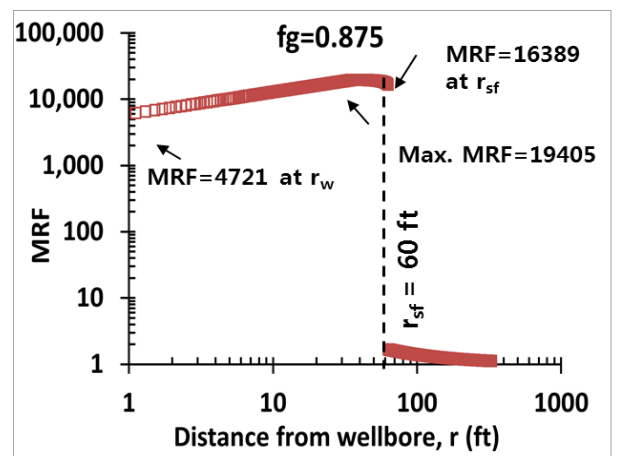
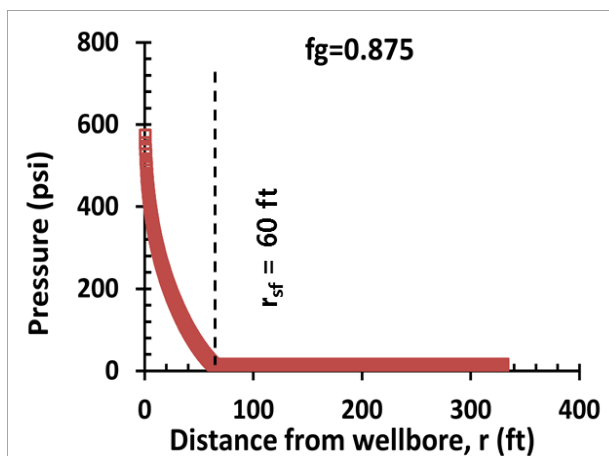


Fig. 4.26(c) Pressure and MRF profiles along the reservoir at  $f_g=0.875$  (grid block size 0.2 ft rather than 2 ft)

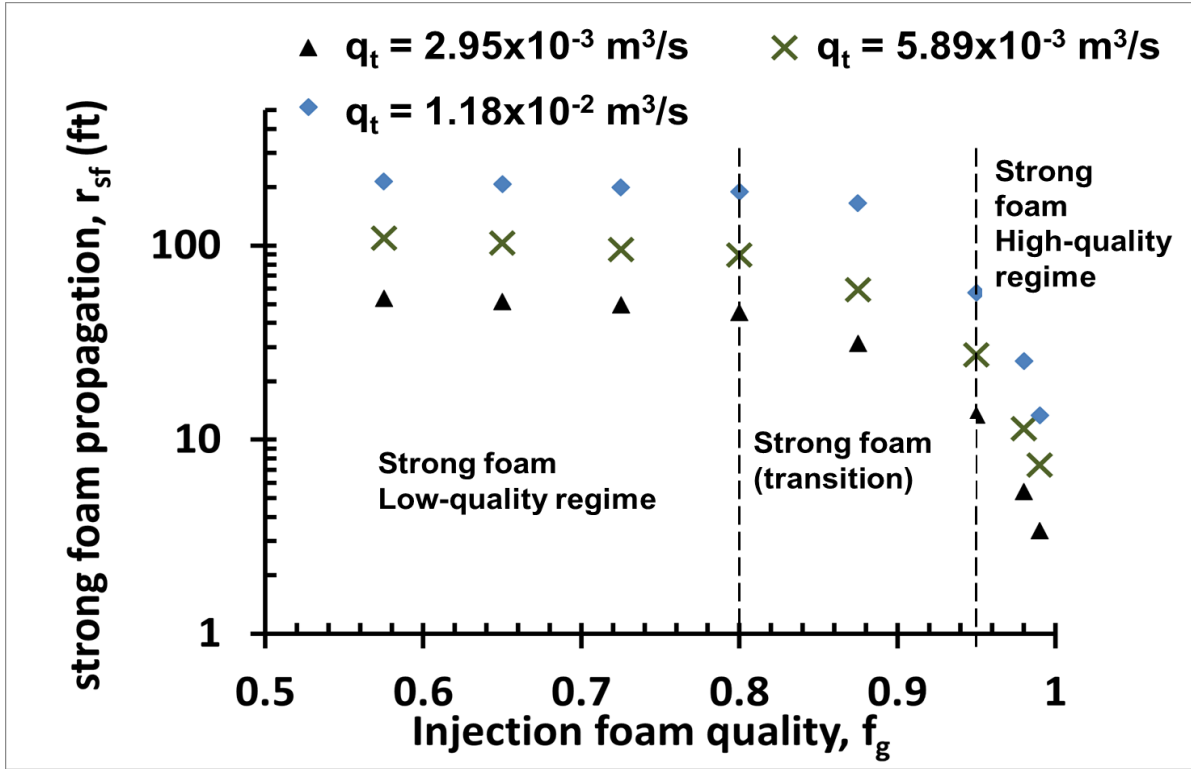
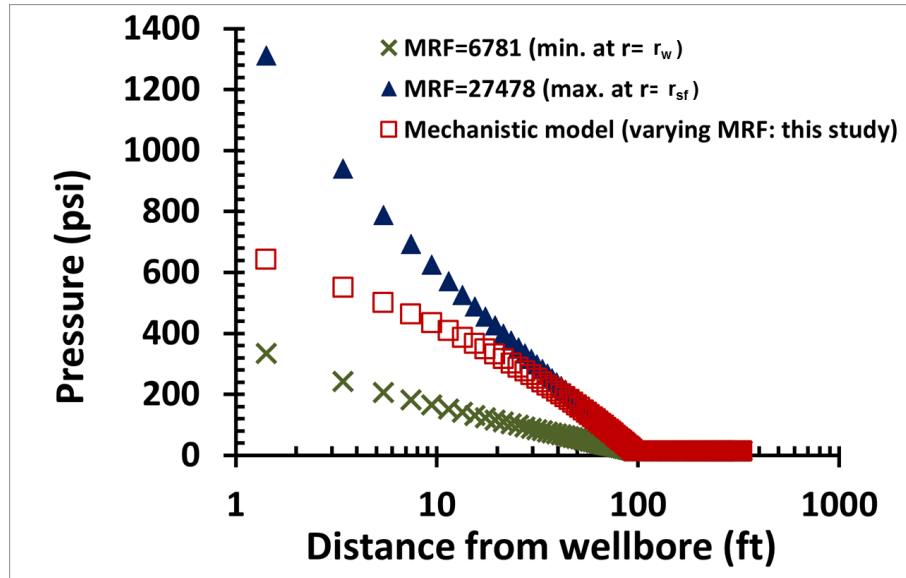
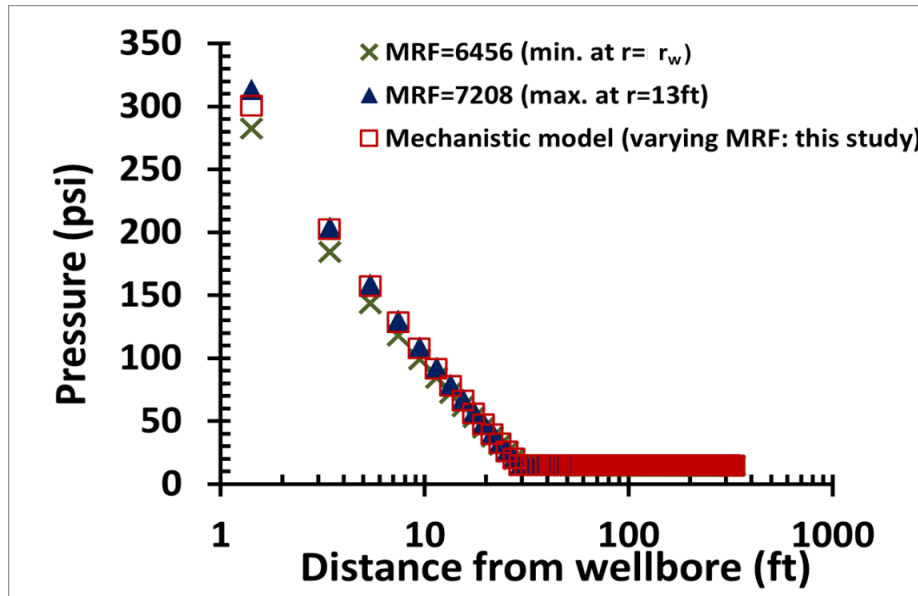


Fig. 4.27 The distance for strong foams to travel before turning into weak foams ( $r_{sf}$ ) as a function of foam quality ( $f_g$ ) and injection rates ( $q_t$ )

Similar to Figs. 4.23 through 4.28 where foams are injected at a pre-specified injection rate ( $q_t$  and  $f_g$  fixed), the same calculations can be performed for foam injection at a pre-specified injection pressure ( $P_{in}$  and  $f_g$  fixed). Fig. 4.29(a) shows the results at various inlet pressure ranging from 2060 to 8660 psia at  $f_g = 0.80$  (low-quality regime),  $r_w = 5$  ft,  $r_e = 330$  ft, and  $P_{out} = 2000$  psia. The results show that higher injection pressure corresponds to higher injection rate and longer distance for strong foams to travel. Fig. 4.29(b) shows more details about  $r_{sf}$  at different injection  $f_g$  values ( $f_g = 0.80, 0.725$ , and  $0.65$ ). Irrespective of  $f_g$  values,  $r_{sf}$  increases dramatically as injection rate or pressure increases. In fact, the use of injection pressure of 4600 psia can make strong foams propagate throughout the system ( $r_{sf} = r_e$ ). The responses at the three  $f_g$  values look quite similar, once again, showing how insensitive  $r_{sf}$  is for foams in the low-quality regime.



(a)

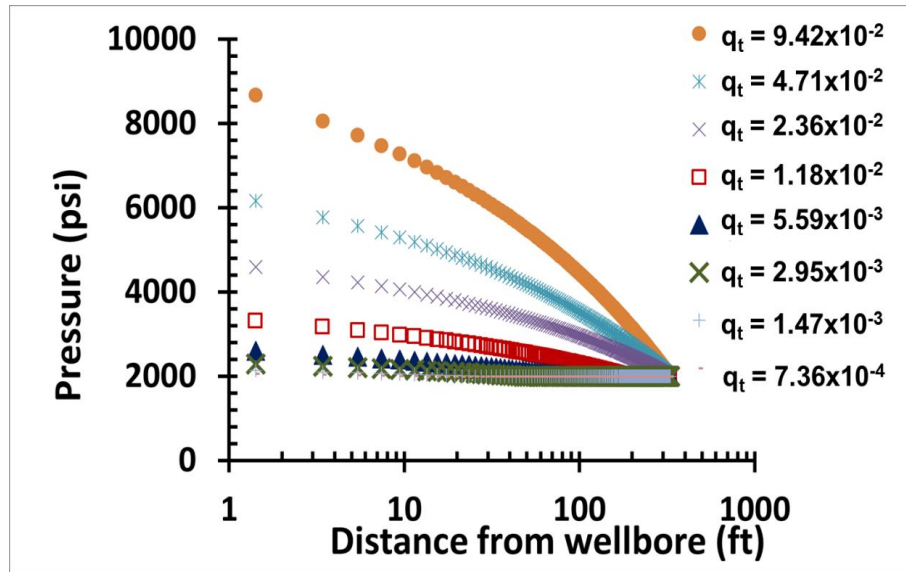


(b)

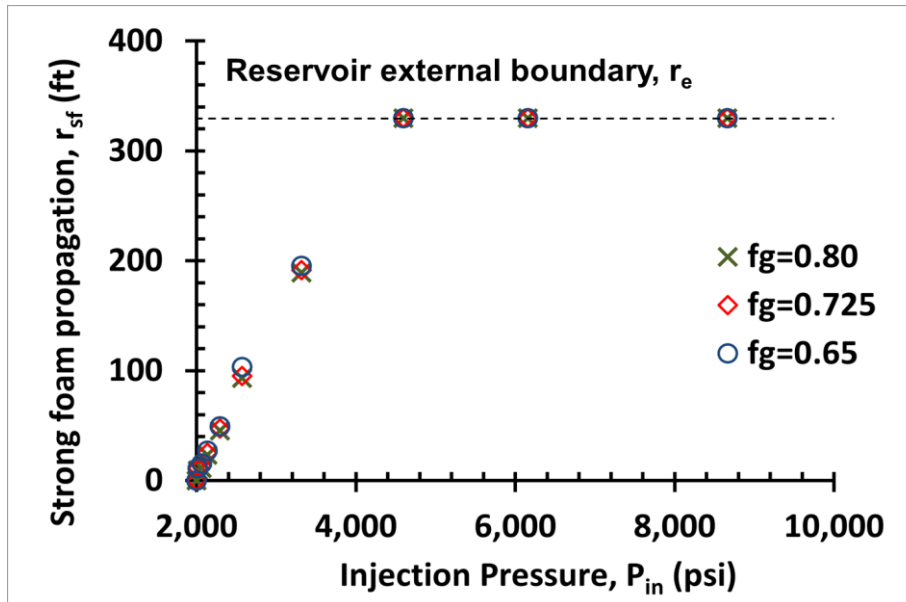
Fig. 4.28 Pressure profile comparing mechanistic model and constant-MRF model: (a) strong foams in the low-quality regime ( $f_g = 0.80$ ) and (b) strong foams in the high-quality regime ( $f_g = 0.95$ )

The same calculations are carried out in Fig. 4.30(a) at  $f_g = 0.95$  (high-quality regime). The results show a similar pattern as in Fig. 4.29(a), but it looks more difficult to make strong foams in the high-quality regime to propagate deep into the reservoir. That aspect is shown

more clearly in Fig. 4.30(b) at  $f_g = 0.98$  and  $0.99$  where foams do not reach the end of the reservoir even at 8000 psia injection pressure. Figs. 4.29 and 4.30 are believed to provide a useful guideline for fixed-pressure foam injection processes in the field.

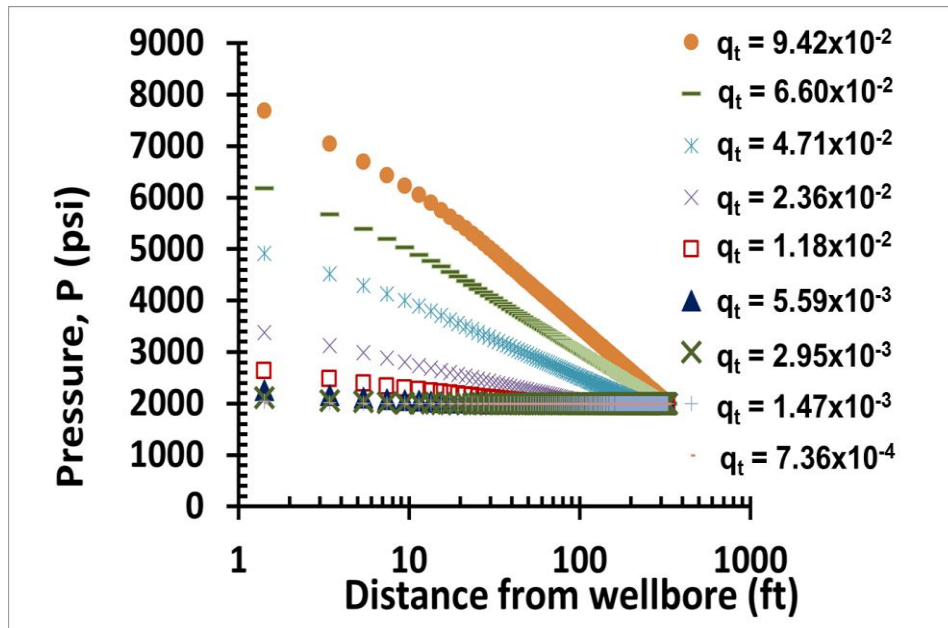


(a)

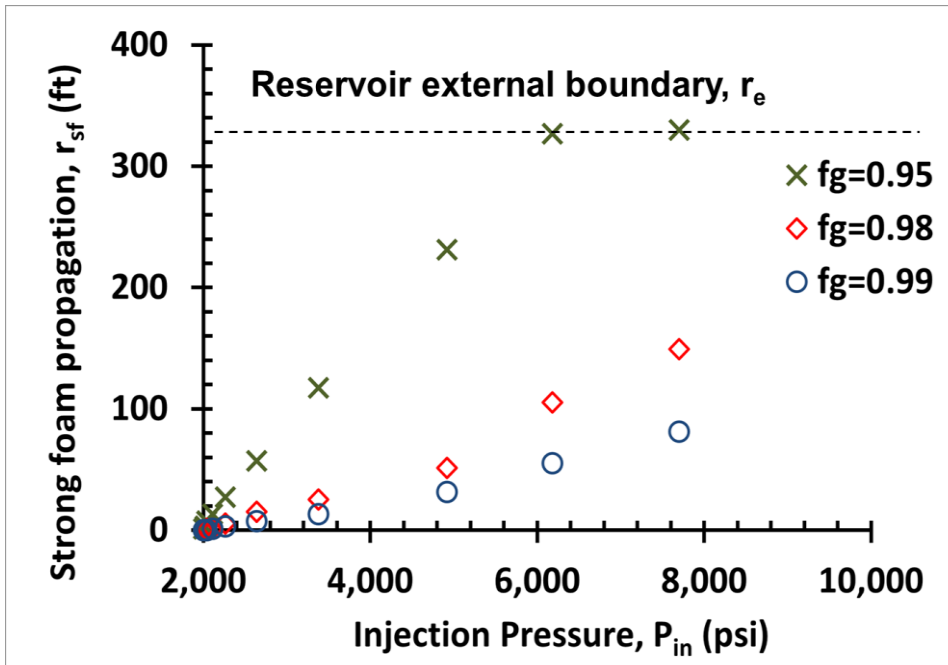


(b)

Fig. 4.29 Foam propagation at fixed injection pressure and foam quality ( $f_g = 0.80$ ,  $r_w = 5$  in ,  $r_e = 330$  ft ,  $P_{out} = 2000$  psia): (a) pressure profile at various inlet pressure (2060 to 8660 psia) and (b) the distance for strong foams to travel before turning into weak foams ( $r_{sf}$ )



(a)



(b)

Fig. 4.30 Foam propagation at fixed injection pressure and foam quality ( $f_g = 0.95$ ,  $r_w = 5$  in,  $r_e = 330$  ft,  $P_{out} = 2000$  psia): (a) pressure profile at various injection pressure (2020 to 7700 psia) and (b) distance for strong foams to travel before turning into weak foams ( $r_{sf}$ ) vs. injection pressure

## CHAPTER 5. CONCLUSIONS

It has been an open question how foam rheology measured in one-dimensional linear system could be translated into that in different geometries and dimensionalities. This study investigated how foam would propagate in non-linear geometries (such as radial and spherical), compared to linear geometry, by using a mechanistic foam model that could deal with three foam states (weak-foam, intermediate, and strong-foam states) and two steady-state strong-foam regimes (high-quality and low-quality regimes). This study first examined foam propagation in a small-scale system, and then moved on to field-scale applications.

1. When the propagation of strong foams was investigated in a small-scale radial system, the results were quite different depending on which flow regime the conditions fall in. For strong foams in the low-quality regime, foam mobility decreased with radial distance (or mobility reduction factor (MRF) increased with radial distance, equivalently), while for strong foams in the high-quality regime, foam mobility decreased with radial distance only near the well, but increased with radial distance away from the well. The results for weak-foam propagation showed that foam mobility increased with radial distance. These findings imply that the use of a fixed MRF may not be appropriate for foam EOR modeling (which is a common practice currently), especially for strong foams in the low-quality regime.
2. When the results in a small-scale spherical system were analyzed, the general trend was shown to be similar to those in a small-scale radial system, but the effect was more pronounced. The model showed that the resistance during foam

- flow in about 1 ft long spherical system was about 4.5 to 5.3 times less, compared to that in 1 ft long linear system, which is similar to the ratio measured by Li et al. (2006) in their cubic sandpack experiments showing the ratio around 5.
3. In large field-scale modeling, it was necessary to estimate upfront the radial distance for injected strong foams to propagate before turning into weak foams ( $r_{sf}$ ) that essentially impacted pressure profile and sweep efficiency. Strong foams were shown to always propagate more at higher injection rates no matter what injection foam qualities were applied. If injection rate was kept constant, foams in the lower injection foam quality led to deeper foam propagation; the effect was significant for foams in the high-quality regime while negligible for foams in the low-quality regime, however.
  4. As far as strong-foam propagation distance ( $r_{sf}$ ) is concerned, an example case taken from a field case (reservoir radius 330 ft, reservoir thickness 27.5 ft) showed that foam could propagate throughout the reservoir with a reasonable injection pressure. For foams in the high-quality regime, much higher injection pressure was shown to be needed to improve strong foam propagation. If all conditions kept the same, foams could propagate more for thinner system.
  5. This study does not consider the presence of oil in the reservoir, nor does it take the effect of compressibility into account. These remain as future research topics.



## REFERENCES

1. Ashoori, E., Marchesin, D., & Rossen, W. R. (2012, January). Multiple Foam States and Long Distance Foam Propagation in EOR Displacements. In SPE Improved Oil Recovery Symposium. Society of Petroleum Engineers.
2. Acton, F. S. Numerical Methods That Work, 2nd printing. Washington, DC: Math. Assoc. Amer., p. 16, 1990.
3. Afsharpoor, A., Lee, G. S., & Kam, S. I. (2010). Mechanistic simulation of continuous gas injection period during surfactant-alternating-gas (SAG) processes using foam catastrophe theory. Chemical Engineering Science, 65(11), 3615-3631.
4. Aronson, A. S., Bergeron, V., Fagan, M. E., & Radke, C. J. (1994). The influence of disjoining pressure on foam stability and flow in porous media. Colloids and Surfaces A: Physicochemical and Engineering Aspects, 83(2), 109-120.
5. Alvarez, J. M., Rivas, H. J., & Rossen, W. R. (2001). Unified model for steady-state foam behavior at high and low foam qualities. SPE journal, 6(03), 325-333.
6. Bernard, G. G., & Jacobs, W. L. (1965). Effect of foam on trapped gas saturation and on permeability of porous media to water. Society of Petroleum Engineers Journal, 5(04), 295-300.
7. Buckley, S. E., & Leverett, M. C. (1941). Mechanism of fluid displacement in sands. Trans. Aime, 146.
8. Holbrook, O. C. (1958). U.S. Patent No. 2,866,507. Washington, DC: U.S. Patent and Trademark Office.
9. Dholkawala, Z. F., Sarma, H. K., & Kam, S. I. (2007). Application of fractional flow theory to foams in porous media. Journal of Petroleum Science and Engineering, 57(1), 152-165.
10. Falls, A. H., Hirasaki, G. J., Patzek, T. E. A., Gauglitz, D. A., Miller, D. D., & Ratulowski, T. (1988). Development of a mechanistic foam simulator: the population balance and generation by snap-off. SPE reservoir engineering, 3(03), 884-892.
11. Friedmann, F., Chen, W. H., & Gauglitz, P. A. (1991). Experimental and simulation study of high-temperature foam displacement in porous media. SPE reservoir engineering, 6(01), 37-45.

12. Friedmann, F., Smith, M. E., Guice, W. R., Gump, J. M., & Nelson, D. G. (1994). Steam-foam mechanistic field trial in the midway-sunset field. *SPE Reservoir Engineering*, 9(04), 297-304.
13. Gauglitz, P. A., Friedmann, F., Kam, S. I., & Rossen, W. R. (2002). Foam generation in homogeneous porous media. *Chemical Engineering Science*, 57(19), 4037-4052.
14. Hirasaki, G. J., & Lawson, J. B. (1985). Mechanisms of foam flow in porous media: apparent viscosity in smooth capillaries. *Society of Petroleum Engineers Journal*, 25(2), 176-190.
15. Holm, L. W. (1970). Foam Injection Test in the Siggins Field Illinois. *Journal of Petroleum Technology*, 22(12), 1-499.
16. Harpole, K. J., Siemers, W. T., & Gerard, M. G. (1994, January). CO<sub>2</sub> Foam Field Verification Pilot Test at EVGSAU: Phase IIIC--Reservoir Characterization and Response to Foam Injection. In *SPE/DOE Improved Oil Recovery Symposium*. Society of Petroleum Engineers.
17. Jiménez, A. I., & Radke, C. J. (1989). Dynamic stability of foam lamellae flowing through a periodically constricted pore.
18. Jonas, T. M., Chou, S. I., & Vasicek, S. L. (1990, January). Evaluation of a CO<sub>2</sub> Foam Field Trial: Rangely Weber Sand Unit. In *SPE Annual Technical Conference and Exhibition*. Society of Petroleum Engineers.
19. Khatib, Z. I., Hirasaki, G. J., & Falls, A. H. (1988). Effects of capillary pressure on coalescence and phase mobilities in foams flowing through porous media. *SPE reservoir engineering*, 3(03), 919-926.
20. Kam, S. I., & Rossen, W. R. (2003). A model for foam generation in homogeneous media. *SPE Journal*, 8(04), 417-425.
21. Kam, S. I. (2008). Improved mechanistic foam simulation with foam catastrophe theory. *Colloids and Surfaces A: Physicochemical and Engineering Aspects*, 318(1), 62-77.
22. Kovscek, A. R., & Radke, C. J. (1994). Fundamentals of foam transport in porous media. *ACS Advances in Chemistry Series*, 242, 115-164.
23. Kovscek, A. R., Patzek, T. W., & Radke, C. J. (1997). Mechanistic foam flow simulation in heterogeneous and multidimensional porous media. *SPE JOURNAL-RICHARDSON-*, 2, 511-526.
24. Lake, L. W. (1989). Enhanced oil recovery.

25. Li, B., Hirasaki, G. J., & Miller, C. A. (2006, January). Upscaling of Foam Mobility Control to Three Dimensions. In SPE/DOE Symposium on Improved Oil Recovery. Society of Petroleum Engineers.
26. Mohammadi, S. S., Van Slyke, D. C., & Ganong, B. L. (1989). Steam-Foam Pilot Project in Dome-Tumbador Midway-Sunset Field. SPE reservoir engineering, 4(01), 7-16.
27. Miller, C. A., & Neogi, P. (Eds.). (2007). Interfacial phenomena: equilibrium and dynamic effects. CRC Press.
28. Ma, K., Lopez-Salinas, J. L., Puerto, M. C., Miller, C. A., Biswal, S. L., & Hirasaki, G. J. (2013). Estimation of parameters for the simulation of foam flow through porous media. Part 1: the dry-out effect. Energy & Fuels, 27(5), 2363-2375.
29. Osterloh, W. T., & Jante Jr, M. J. (1992, January). Effects of gas and liquid velocity on steady-state foam flow at high temperature. In SPE/DOE Enhanced Oil Recovery Symposium. Society of Petroleum Engineers.
30. Ransohoff, T. C., & Radke, C. J. (1988). Mechanisms of foam generation in glass-bead packs. SPE reservoir engineering, 3(02), 573-585.
31. Rossen, W. R., & Gauglitz, P. A. (1990). Percolation theory of creation and mobilization of foams in porous media. AIChE Journal, 36(8), 1176-1188.
32. Rossen, W. R., & Wang, M. W. (1999, June 1). Modeling Foams for Acid Diversion. Society of Petroleum Engineers. doi:10.2118/56396-PA
33. Sanders, A., Jones, R. M., Rabie, A., Putra, E., Linroth, M. A., & Nguyen, Q. P. (2012, January). Implementation of a CO<sub>2</sub> Foam Pilot Study in the SACROC Field: Performance Evaluation. In SPE Annual Technical Conference and Exhibition. Society of Petroleum Engineers
34. Stevens, J.E. (1995). CO<sub>2</sub> Foam Field Verification Pilot Test at EVGSAU: Phase IIIB-- Project Operations and Performance Review. SPE Res Eng 10 (4): 266-272. SPE-27786-PA. <http://dx.doi.org/10.2118/27786-PA>
35. Wan-Mohamad, W. N., Abdullah, M. A. Y., Selamat, S. B., & Elias, M. R. (2005, January). Application of Improved and Enhanced Oil Recovery Strategies in the Tapis Field. In SPE International Improved Oil Recovery Conference in Asia Pacific. Society of Petroleum Engineers.

## **VITA**

Woochan Lee is the second son of Jongbok Lee and Taeok Im, and the head of his own family with a lovely wife name, Juyun Lee, and a boy to be born in January of 2015. He graduated from University of Texas at Austin in May of 2010 and worked at Korea National Oil Corporation (KNOC) after graduation until he began his study at Louisiana State University in August of 2012. He is specialized in reservoir and production engineering throughout his full time and internship in KNOC and RWE Dea AG. He is interested in traveling and has a plan to travel 20 countries with his parents and family by the year of 2030.